Extraction of $A_{LU}^{sin(\phi)}$ moments from the hard exclusive π^+ channel off the unpolarized hydrogen target in a wide range of kinematics

Stefan Diehl[1,2*], David Riser[1], Kyungseon Joo[1], Kijun Park[3]

[1]University of Connecticut
[2]Justus Liebig University Giessen
[3]Yorktown, Virginia 23692

August 2018

Abstract

For the first time, we have measured single beam spin asymmetries to extract $A_{LU}^{sin(\phi)}$ moments from the hard exclusive π^+ channel off the unpolarized hydrogen target in a wide range of kinematics from forward angles to backward angles in CM. The forward angle is known to be sensitive to generalized parton distributions (GPDs) and the backward angle is known to be sensitive to transition distribution amplitudes (TDAs). Our results clearly show that the sign of forward BSA measurements is positive wheres that of backward BSA measurements is negative while the sign transition takes place near 90 degree in CM. By making accurate measurements over a wide range of Q^2 and t, we can explore the transition from the hadronic to partonic reaction mechanisms.

Contents

1 Introduction **1**

2 Experimental Setup **3**
2.1 CEBAF 3
2.2 The CLAS detector in hall B 3
2.2.1 The torus magnet and drift chambers 3
2.2.2 The Cherenkov counter 4
2.2.3 The time of flight system 4
2.2.4 The electromagnetic calorimeter 4
2.3 The e1-f run 4

3 Data Quality and Corrections **5**
3.1 Determination of a list of good runs 5
3.2 Determination of the electron beam helicity 5
3.3 Vertex correction 6
3.4 Timing correction 7
3.5 Kinematic corrections 9

4 Particle Identification **13**
4.1 Electron Identification 13
4.1.1 Negative charge condition 14
4.1.2 Drift chamber fiducial cuts 14
4.1.3 Electromagnetic Calorimeter fiducial (UVW) 15
4.1.4 EC minimum energy deposition cut 17
4.1.5 Electromagnet calorimeter sampling fraction cut . . . 18
4.1.6 Cut on the z-vertex position 18
4.1.7 Cherenkov counter θ_{cc} and ϕ_{rel} matching to PMT cuts 20
4.2 Hadron Identification 21
4.2.1 Drift chamber fiducial cut 23

4.2.2 Hadron-electron vertex difference cut 23
4.2.3 β vs p cut and likelihood maximization of $\beta(p,h)$ . . . 23

5 Analysis of the Beam Spin Asymmetry 31
5.1 Introduction 31
5.2 Event selection 31
5.3 Kinematics and Binning 32
5.3.1 Kinematics 32
5.3.2 Binning 36
5.4 Extraction of the BSA 38
5.4.1 Determination of the parameter $A_{LU}^{sin(\phi)}$ and statistical errors 39
5.4.2 Estimation of systematic errors 41
5.4.3 Results and Discussion 46

Bibliography v

Chapter 1

Introduction

According to the collinear factorization theorems of QCD, many hard exclusive reactions can be described in terms of universal nucleon structure functions. These structure functions which depend on different impact parameters and the parton longitudinal momentum can provide us an insight into the complex quark and gluon structure of hadrons. For the description of the exclusive $ep \rightarrow èn\pi^+$ process, different structure functions have to be used for the description, depending on the kinematic region. While the shown QCD factorization mechanism in the "'nearly forward region"' (large Q^2 and small $|t|$) can be divided into a hard part, described by perturbative QCD and in two general structure functions, the GPDs for the nucleon and the pion DA, describing the complex non perturbative structure of these particles, the "'nearly backward"' kinematic region (Q^2 and W^2 are small, x_B is fixed and $|u|$ is small) has to be described by a convolution of the non-perturbative nucleon-to-pion transitions (TDAs), the nucleon DA and the hard interaction amplitude from perturbative QCD [PGG18]. The reaction mechanisms are illustrated in figure 1.1

The paper presents a study of the forward - backward asymmetry of the $sin(\phi)$ moment of the cross section $A_{LU}^{sin(\phi)}$ of exclusive deeply virtual pion electro production of the proton $ep \rightarrow e\pi^+n$, extracted from fits to beam-spin asymmetries (BSAs). The sign change of the $A_{LU}^{sin(\phi)}$ during the transition between forward and backward region indicates the transition between a GPD based transition description and a TDA based description for the different kinematic regions.

The cross section of the exclusive pion electroproduction can be described by:

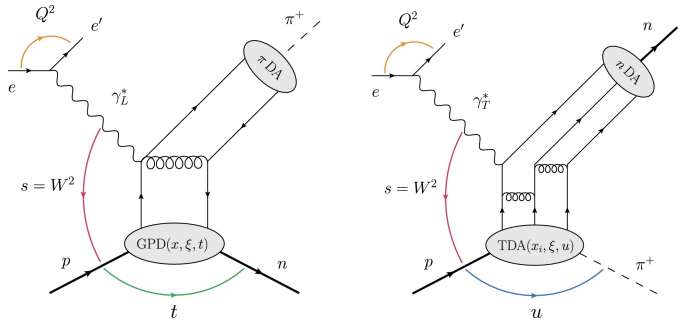

Figure 1.1: Left: Exclusive electroproduction of a pion on the proton in the "nearly forward region" (large Q^2 and small $|t|$). The shown QCD factorization mechanism can be divided into a hard part, described by perturbative QCD and in two general structure functions, the GPDs for the nucleon and the pion DA, describing the complex non perturbative structure of these particles. Right: Factorisation of the same reaction in the "nearly backward" kinematic region (Q^2 and W^2 are small, x_B is fixed and $|u|$ is small). In this region, the process can be described by a convolution of the non-perturbative nucleon-to-pion transitions (TDAs) and the nucleon DA and the hard interaction amplitude from perturbative QCD. [PGG18]

$$\frac{d^4\sigma}{dQ^2 dx_B d\phi dt} \approx \sigma_T + \epsilon_L \sigma_L + \epsilon \sigma_{TT} \cdot cos(2\phi) + \sqrt{2 \cdot \epsilon_L \cdot (1+\epsilon)} \cdot \sigma_{LT} \cdot cos(\phi) + h \cdot \sqrt{2 \cdot \epsilon_L \cdot (1-\epsilon)} \cdot \sigma_{L\hat{T}} \cdot sin(\phi) \tag{1.1}$$

with the linear and longitudinal polarization parameters ϵ and ϵ_L of the virtual photon and the beam polarization h.

Based on this cross section, the beam spin asymmetry can be derived as:

$$BSA = \frac{\sigma^+ - \sigma^-}{\sigma^+ + \sigma^-} \propto \frac{\sigma_{L\hat{T}}}{\sigma_T + \epsilon_L \sigma_L} \cdot sin(\phi) = A_{LU}^{sin(\phi)} \cdot sin(\phi) \tag{1.2}$$

Considering also higher order momenta, the BSA is given by:

$$BSA = \frac{\sigma^+ - \sigma^-}{\sigma^+ + \sigma^-} = \frac{A_{LU}^{sin(\phi)} \cdot sin(\phi)}{1 + A_{LU}^{cos(\phi)} \cdot \cdot cos(\phi) + A_{LU}^{cos(2\phi)} \cdot \cdot cos(2\phi)} \tag{1.3}$$

Chapter 2

Experimental Setup

The following chapter will shortly describe the experimental setup used for this study.

2.1 CEBAF

The experiment was performed in hall B at Jefferson National Lab (JLAB). To produce a high energetic electron beam, JLAB operates the continuous electron beam accelerator facility (CEBAF). During the time of the e1-f run period in 2003 the accelerator was able to provide a 6 GeV electron beam.

2.2 The CLAS detector in hall B

The analyzed data was recorded with the CEBAF large acceptance spectrometer (CLAS), operated in Hall B. The CLAS detector was designed to detect particles over a very large angular range, covering almost the full 4π solid angle around the target region. Besides this angular coverage, also a high efficiently for the detection of particles with a wide range of momenta between 0.5 - 6.0 GeV was one of the design goals.

2.2.1 The torus magnet and drift chambers

The momentum measurement of charged particles with p $>$ 200 MeV/c was performed by measuring the curvature of the particle trajectory as it passed through the CLAS toroidal magnetic field. Six superconducting coils were arranged 60° apart azimuthal around the beam-line to create a 2 Tesla magnetic field. In order to perform tracking before, inside, and after the

torus three radially distinct drift chambers were constructed for each sector (these were called regions 1, 2, and 3), leading to a total of 18 drift chambers for the 6 sectors.

2.2.2 The Cherenkov counter

The Cherenkov counters (CC) are located radially outside of the region 3 drift chambers. They provide a separation of electrons and negatively charged pions for tracks with momentum less than the pion momentum threshold $p < p_\pi \approx 2.5$ GeV/c [GA01]. Like the drift chambers, also the Cherenkov counters were divided into 6 sectors. Each sector was divided into 18 segments in the polar angle θ away from the beamline. Each of these segments was divided in half azimuthally to produce 12 half-sectors.

2.2.3 The time of flight system

For the identification and separation of hadrons, especially in the low momentum region, the measurement of the flight time over a known distance is a powerful tool, since for a particle with known momentum (measured in the drift chambers) the average velocity is directly correlated to its mass. However due to the limited time resolution, this method is restricted to the region of low momenta. Operating on this principle the CLAS time of flight (TOF) system allowed for the separation of π and K for momentum p $\leq$ 2 GeV/c.

2.2.4 The electromagnetic calorimeter

The electromagnetic calorimeter (EC) was the outermost layer of the CLAS detector. This sampling calorimeter was a main component of the CLAS trigger. Its primary role was to detected and trigger on electrons with E $>$ 0.5 GeV. In addition neutral particles such as photons and neutrons could be detected.

2.3 The e1-f run

This study uses the dataset collected between April and July of 2003 known as e1-f. During this run period the beam energy was 5.498 GeV and the unpolarized target was a 5cm liquid hydrogen cell. The torus current was set to 2250 Amperes, to maximize pion acceptance. The average electron beam polarization has been measured to be 75 $\pm$ 2.4 %.

Chapter 3

Data Quality and Corrections

This chapter discusses the data quality control, the determination of the beam helicity as well as the correction of different reconstructed properties. To guarantee a reliable dataset, vertex corrections, timing corrections and kinematic corrections have to be applied.

3.1 Determination of a list of good runs

The total data set contains 831 runs. Due to the complexities of the CLAS experimental setup, it is not uncommon for run conditions to change during a small percentage of the runs such that the data collected are not of analysis quality. For this reason, a list of runs with acceptable and well defined properties has to be determined. Good runs are selected by comparing the number of good electrons, normalizing by the accumulated charge in each file. Figure 3.1 histograms the described ratio for all runs.

While the number of events collected varies from run to run, the ratio defined above is a stable quantity - provided that the run conditions do not vary greatly. Runs which are within 3 standard deviations of the mean (calculated over the dataset) are used as good runs. The good run list used for this analysis contains 522 runs.

3.2 Determination of the electron beam helicity

To minimize systematic effects, the beam helicity convention was changed several times during the e1-f run period by the insertion of a half-wave plate

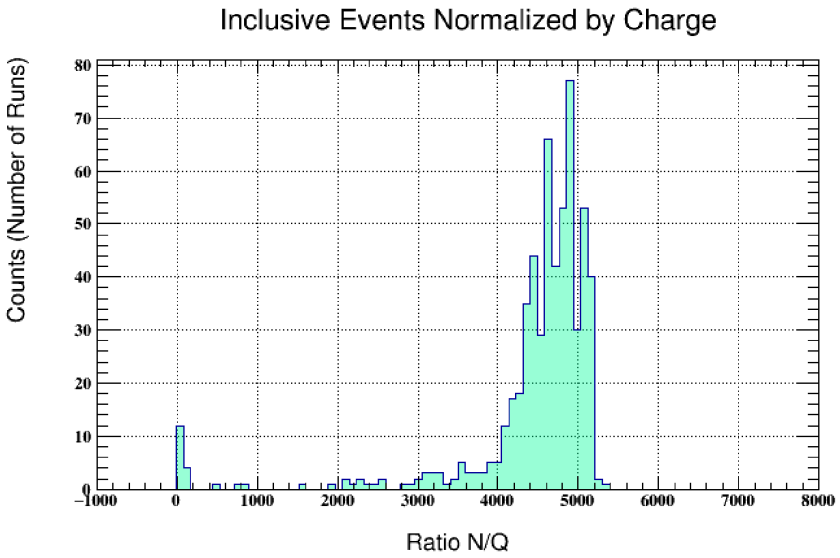

Figure 3.1: Inclusive electrons per file normalized by the total charge accumulated for the file. This quantity is used to make a good run list.

at the injector. The definition of ± helicity must change in accordance with these wave-plate insertions. To monitor these changes, the value of $A_{LU}^{sin(\phi)}$ for π^+ is recorded for every run. Whenever the asymmetry (which has a magnitude of around 3%) changes its sign, the sign convention has changed. These changes are taken into account in the data analysis. Figure 3.2 shows the BSA for all runs before and after the half wave plate correction.

3.3 Vertex correction

The track vertex position (v_x, v_y, v_z) is calculated based on the intersection of each track with the midplane (the plane which contains the beamline and bisects the sector at $\phi_{rel} = 0$). If the beam is not centered at (x, y) = (0.0, 0.0), the vertex position calculation needs to be corrected by shifting the midplanes in accordance with the target offset. The offset (x, y) is identified by plotting events from the control foil placed near the target, which has a z position of -20 cm. For the e1-f run period, the beam position was (0.15, -0.25) cm.

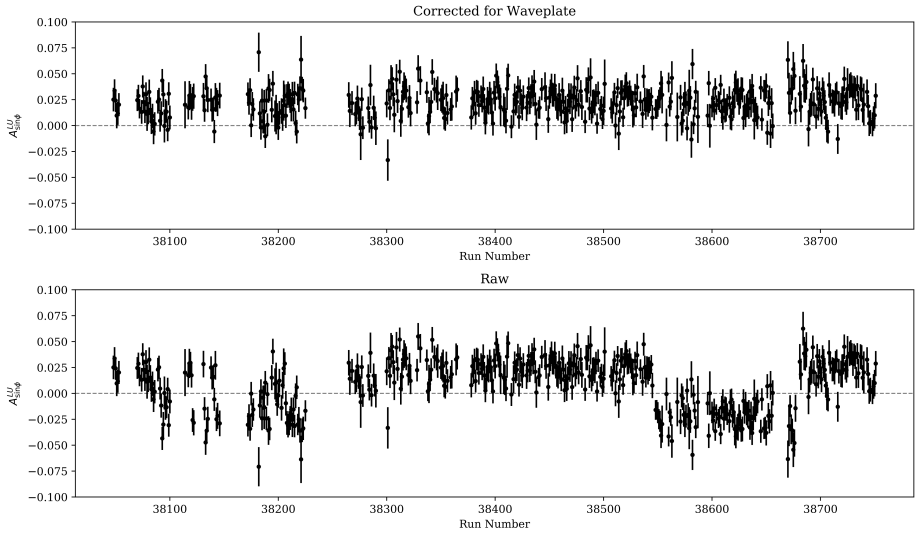

Figure 3.2: The half wave plate position is determined and corrected by plotting the BSA for π^+ mesons as a function of the run. The top panel shows the corrected results, the bottom shows the results before changing the helicity.

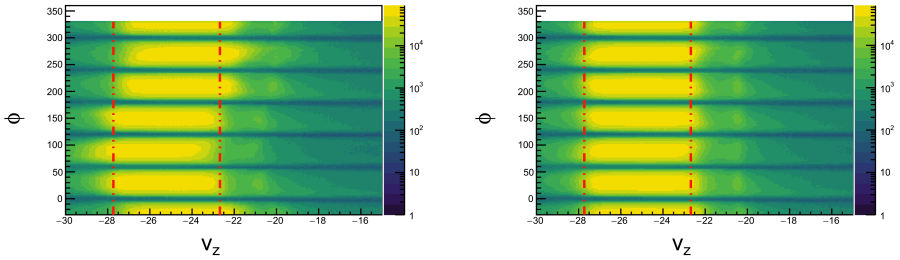

Figure 3.3: The z-vertex position v_z shown for different values of the azimuthal angle ϕ in the hall. The left figure shows the distribution before corrections are applied, the right after. The vertical red lines bound the region which we define as acceptable for electrons in our analysis.

3.4 Timing correction

The timing information is extracted from the PMT signals of the time-of-flight detector system. For the e1-f dataset it was found, that even after a time calibration of the TOF, small offsets in timing between time of flights

paddles still exist, with a variation over the run period. These biases can be removed on a run-by-run and paddle-by-paddle basis by adding a small shift t_{corr} to the initial time of the paddle. In order to determine this shift t_{corr} for each paddle, charged pions are used. Based on the momentum information from the drift chambers the expected value of β can be calculated for each pion. The required correction is proportional to the difference $\Delta\beta$:

$$\Delta\beta = \beta_{obs} - \beta_{calc} = \frac{d}{c \cdot t_{obs}} - \sqrt{1 + (m_\pi/p)^2} \tag{3.1}$$

The offset $\Delta\beta$ from 0 is used to define the value of t_{corr} for each paddle. If this value is exceedingly small, no correction is applied. For some paddles with low statistics a reasonable value for t_{corr} cannot be obtained. To exclude an uncontrolled behavior, these paddles are excluded from the analysis.

In the method described above, the calibrated paddle is the one which is crossed by the pion. However, the electron paddle which was hit by the electron which determined the start time may also require calibration. In practice the magnitude of the correction term t_{corr} is small, and the paddle offset is (likely) randomly distributed around 0 when considering all paddles. By including events from many different (electron) paddles, miss-calibration effects from the electron side average out for the mean value of the offset distribution. The success of the method is demonstrated by the centering of the $\Delta\beta$ distributions in figure 3.4. The method was first described in [NAH10].

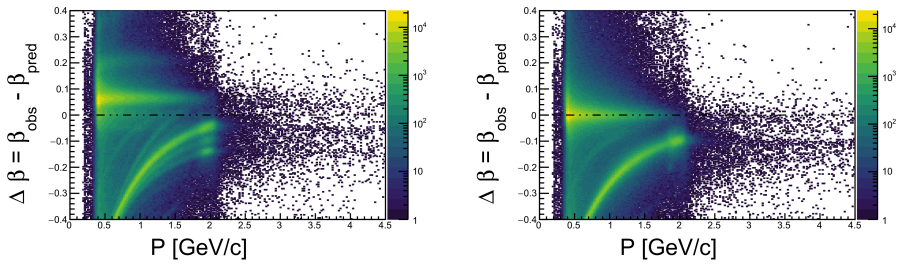

Figure 3.4: Timing corrections are shown for paddle 24 of sector 1. The left image shows the $\Delta\beta$ distribution before corrections. On the right the same is shown after correction of the timing for this paddle. We assume the mass of the track to be the pion, these show up as the green band. Heavier protons are visible below the pion band.

3.5 Kinematic corrections

The magnetic field map used in reconstruction to swim particle tracks cannot perfectly match the real magnetic field of the hall. As a result of this the reconstructed momentum of particles is often slightly off ($\approx 1\%$). Small misalignment in detector positions also contribute to this effect. Figure 3.5 shows the deviation of the elastic e p $\rightarrow$ e p events in the W spectrum from the expected value of the proton mass.

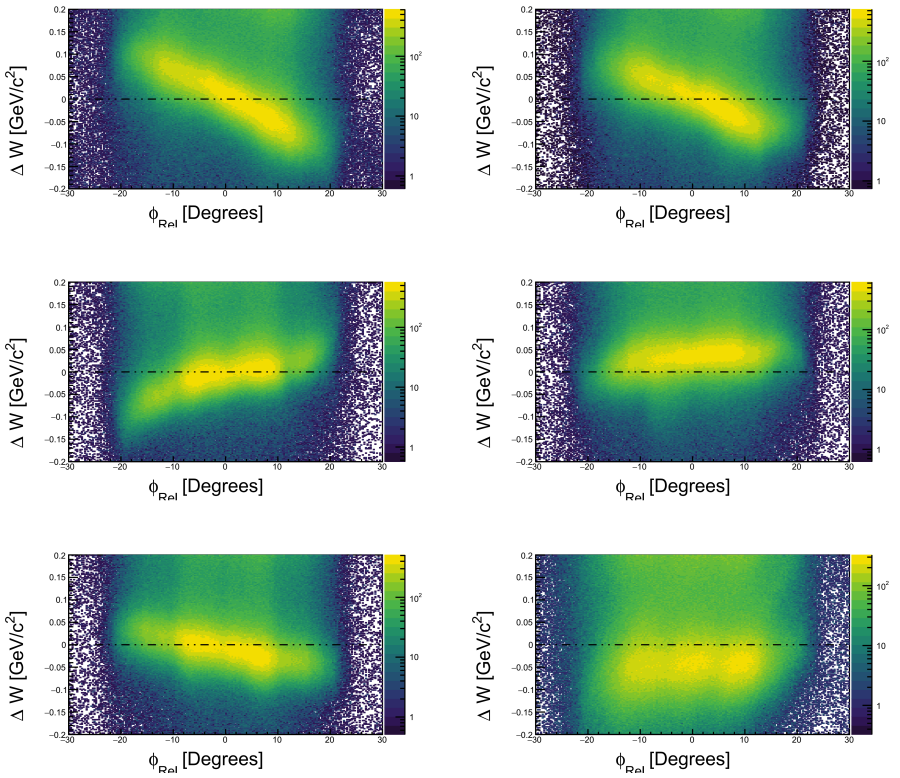

Figure 3.5: Deviation of the elastic e p $\rightarrow$ e p events in the W spectrum from the expected value of the proton mass (before corrections).

In order to correct for these small differences, the momentum (p_x, p_y, p_z) and hence θ of charged tracks is corrected. For the correction of kinematic variables of measured particles several methods have been established. However, all of them rely on energy and momentum conservation applied to standard processes like elastic scattering. The procedure used to derive corrections for the e1-f dataset was developed and described by Marco Mi-

razita in [MM]. The need for correction to θ (the polar angle measured from the beamline) results from miss-alignments in the drift chambers. Since this implies that the correction is the same for positives and negatives, this assumption has been used in the correction algorithm. First, elastic (ep $\rightarrow$ ep) events are selected by identifying events that contain at least one electron and one proton, then requiring that the missing mass MX of the (ep $\rightarrow$ epX) system is close to 0. The kinematics of the event are then calculated as follows:

$$k^{\mu} = (k, 0, 0, k) \tag{3.2}$$

$$p^{\mu} = (m_p, 0, 0, 0) \tag{3.3}$$

$$k^{'\mu} = (k^{'}, k^{'} \cdot sin(\theta), 0, k^{'} \cdot cos(\theta)) \tag{3.4}$$

$$p^{'\mu} = (p^{'}, p^{'} \cdot sin(\alpha), 0, p^{'} \cdot cos(\alpha)) \tag{3.5}$$

The application of energy and momentum conservation to the equations above leads to:

$$k + m_p = k^{'} + \sqrt{m_p^2 + p^{'2}} \tag{3.6}$$

$$k^{'} \cdot sin(\theta) = p^{'} \cdot sin(\alpha) \tag{3.7}$$

$$k = k^{'} \cdot cos(\theta) + p^{'} \cdot cos(\alpha) \tag{3.8}$$

Based on these equations, the electron angle θ and the proton angle α can be predicted by using the momenta (k_0, p_0).

$$cos(\theta) = 1 - m_p \frac{k - k^{'}}{k k^{'}} \tag{3.9}$$

$$tan(\alpha) = \frac{1}{p^{'}} \frac{k^{'} \cdot sin(\theta)}{k - k^{'} \cdot cos(\theta)} \tag{3.10}$$

These values are compared with measured values and iteratively corrected by tuning the parameters of a ϕ-dependent 2nd order polynomial.

After the application of the θ correction, also the momentum of the electron is corrected by using an analogous procedure for k_0 instead of θ and α. The momentum corrections are calculated as functions of ϕ for each sector in one degree θ bins.

In a last step, the positively charged particles momenta are corrected by selecting the exclusive event (ep $\rightarrow$ e π^+ N). In this reaction the scattered electron and pion are detected and the neutron is selected using a missing mass cut. Assuming the electron momentum, electron angle, and pion angle

to be correct. The pion momentum correction is calculated by iteratively improving the central position of the neutron mass peak to coincide with the neutron mass. Marco Mirazita shows in his note that these corrections can be satisfactorily applied to all negative and positive particles. Figure 3.6 shows the effect of the corrections on the distributions from figure 3.5. The effect of the correction which turns the ϕ sloped distribution into a straight band around zero can be nicely observed.

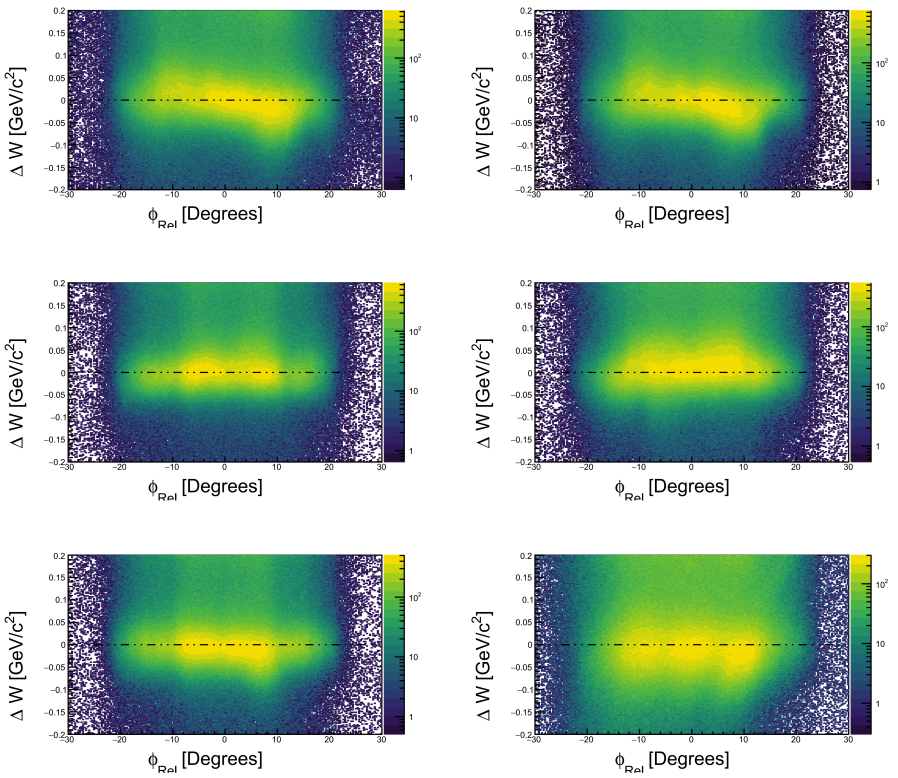

Figure 3.6: Deviation of the elastic e p $\rightarrow$ e p events in the W spectrum from the expected value of the proton mass after the application of ϕ-dependent corrections.

The effect of the kinematic corrections can be also nicely visualized with the distribution of the elastic events in the W spectrum which is shown in figure 3.7 before and after the momentum correction has been applied. The distribution illustrates that the kinematic corrections shift the peak to the correct position and improve its resolution.

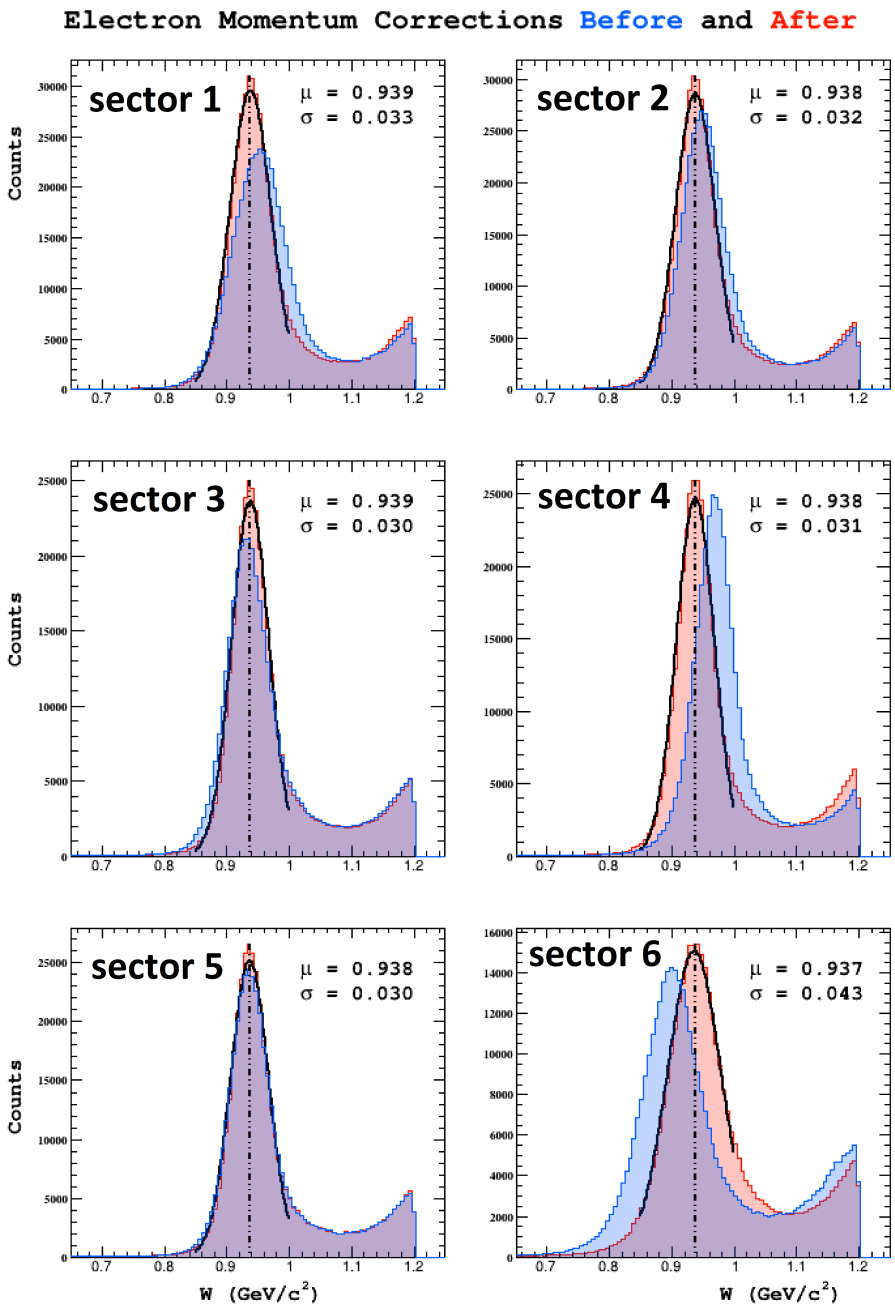

Figure 3.7: Distribution of the elastic events in the W spectrum before and after momentum corrections are applied.

Chapter 4

Particle Identification

After the correction of momentum and time information has been performed, the detected particles can be assigned to their species based on the information provided by the different components of the detector. While the reconstruction package "recsis" of the event-builder assigns a preliminary particle identification based on loose selection criteria, a more reliable particle ID has been implemented in this analysis. The following chapter discusses the single cuts which have been performed to identify a specific particle and to reject potential electronic noise and resulting "fake" tracks.

4.1 Electron Identification

Since an electron scattering experiment has been performed, the detection of the scattered electron in every event is a key requirement for most analyses. For this identification, a compromise between efficiency and accuracy has to be made. On the one extreme, the highest efficiency could be achieved if all negative tracks would be declared as electrons. However this sample would be highly contaminated by negative pions and a significantly lower number of kaons. Therefore cuts have been developed which remove these particles without rejecting too many good electrons.

The cuts used to select electrons are the following:

- Negative charge condition
- Drift chamber region 1 fiducial cut
- Drift chamber region 3 fiducial cut
- Electromagnetic Calorimeter fiducial cut

- Electromagnetic Calorimeter minimum energy deposition cut
- Electromagnet Calorimeter sampling fraction cut
- z-vertex position cut
- Cherenkov counter θ_{cc} matching to PMT number cut
- Cherenkov counter ϕ_{rel} matching to PMT cut (left/right)

In the following paragraphs, the single cuts are motivated and described in more detail.

4.1.1 Negative charge condition

Each track is assigned a charge based on the curvature of its trajectory through the magnetic field of the torus. This is done during the track reconstruction phase. Tracks are eliminated as electron candidates if they are not negatively charged.

4.1.2 Drift chamber fiducial cuts

The fiducial region or volume is a term used to refer to the region of a sensitive detector which is unimpeded in its acceptance of physics events. In practice, shadows from other detectors, poorly understood edge effects, or geometric effects may impede the flight of particles from the target, and render regions of sensitive detectors unreliable. Negative tracks which pass geometrically close to the edges of the drift chamber are, from a tracking perspective, more difficult to understand. Additionally, tracks which fall outside of the fiducial region of the drift chambers are likely to fall outside of the fiducial region of the downstream detectors as well. For these reasons, it is common to remove tracks which are geometrically close to the boundaries of the drift chambers in region 1 and region 3 of the Drift-chambers. Region 2 is not considered for these cut, since most of the events which pass the fiducial cut on the other regions would also pass a fiducial cut on region 2.

To implement this cut the (x, y) coordinates of the drift chambers are rotated into one sector. Then boundaries y_{left}, y_{right} are defined as linear functions of x. The boundary lines are parametrized by an offset h and an angle of the boundary line with respect to the center of the sector at $x = 0$. The slope of these lines is $\pm cot(\theta)$. The borders of the cut are then defined by the following function:

$$y_{right} = h + cot(\theta) \cdot x \tag{4.1}$$

$$y_{left} = h - cot(\theta) \cdot x \tag{4.2}$$

For the two regions, the values of h and θ given in table 4.1 have been determined: Tracks passing this criterion are those which have $y > y_{left}(x)$

region	h (cm)	θ (°)
1	22	60
2	80	49

Table 4.1: Parameters for the Driftchamber fiducial cuts.

and $y > y_{right}(x)$. Figure 4.1 and 4.2 show the applied cuts for DC region 1 and 3.

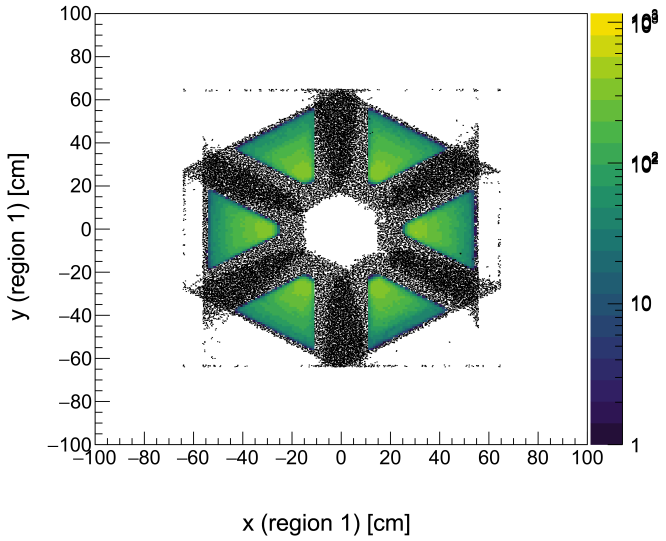

Figure 4.1: Tracks shown in color remain after the application of drift chamber region 1 fiducial cuts to all cuts, shown here as black points.

4.1.3 Electromagnetic Calorimeter fiducial (UVW)

If electrons hit the electromagnetic calorimeter they initiate electromagnetic showers. If the electron hits close to the edges of the detector, there is a chance that the shower will not be fully contained within the calorimeter

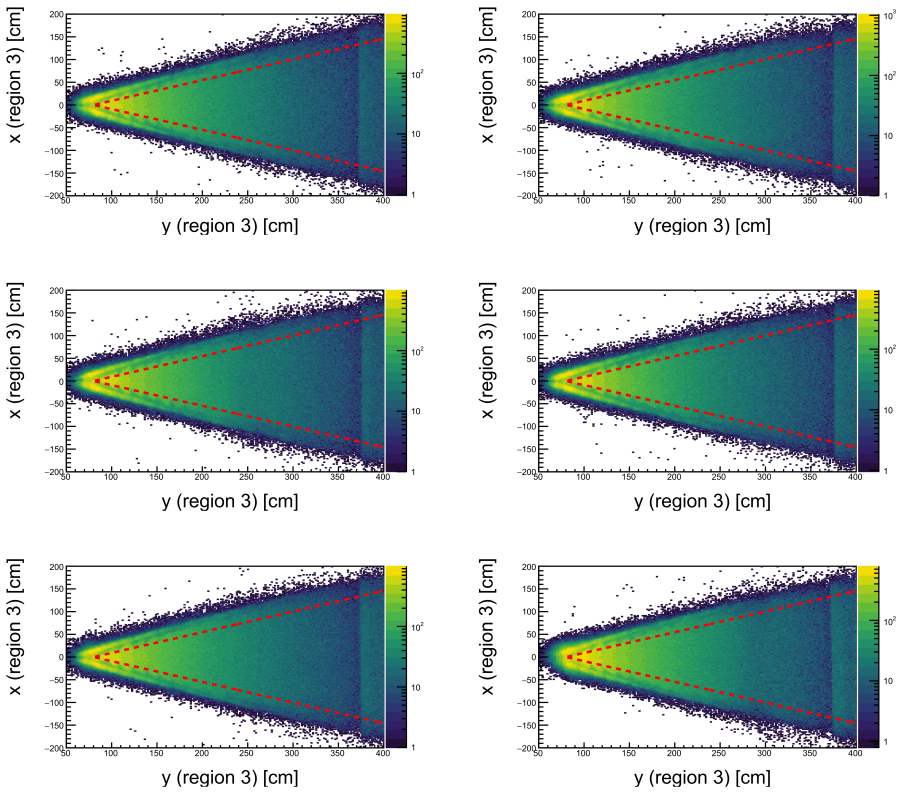

Figure 4.2: All negative tracks are shown here in black. In color, the tracks which pass the EC fiducial cut are shown.

volume. Therefore the reconstructed energy deposition will be reduced and lead to a wrong sampling fraction. For this reason, it is standard to remove the hits which fall within the outer 10 cm of each layer of the EC (10 cm is the width of a scintillator bar). This cut is applied in the u, v, w coordinate system, which gives the natural orientation of the scintillator bars. Table 4.2 summarizes the applied cut values.

EC coordinate	min (cm)	max (cm)
u	70	400
v	-	362
w	-	395

Table 4.2: Parameters for the electromagnetic calorimeter fiducial cuts.

Figure 4.3 shows the effect of the EC fiducial cut on the track selection.

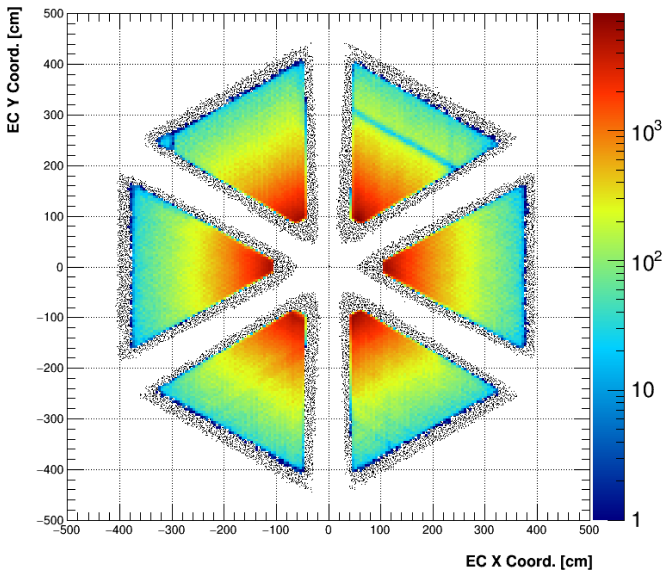

Figure 4.3: The colored area shows the tracks which pass the EC fiducial cut. For comparison, all negative tracks which are outside the fiducial area are shown in black.

4.1.4 EC minimum energy deposition cut

While the fiducial cuts only reject tracks which are not fully or not correctly reconstructed, a first criterion to differentiate between these electrons and pions is to exploit the difference in energy deposition between the two particle species in the electromagnetic calorimeter. Electrons interact electromagnetically and therefore develop an extended electromagnetic shower with a significant energy deposition. In contrast to this, most pions in the investigated energy range are minimal ionizing particles and deposit a constant amount of energy per path length. Especially i the inner part of the calorimeter where the shower reaches its maximal energy deposition, the energy deposited by electrons is significantly larger than the energy deposited by pions. Therefore, this analysis requires that at least 60 MeV was deposited in the inner calorimeter for electron candidates.

4.1.5 Electromagnet calorimeter sampling fraction cut

Since the electromagnetic calorimeter of CLAS6 consist of a sampling structure, only a fraction of the energy is deposited in the active scintillator volume, while most of the energy is lost ion the absorber layers. The Calorimeter is designed in a way that the fraction of the deposited energy by electrons over their momentum, measured by the drift chambers E_{dep}/p is approximately 0.3, independent of their momentum. In contrast to this, the ratio $E_{dep} = p$ for pions decreases rapidly with momentum. To develop a momentum dependent cut for this distribution, all negative candidates are first filled into a two-dimensional histogram of E_{dep}/p vs. p. The histogram is then binned more coarsely in momentum, and projected into a series of 40 momentum slices. Each of these slices is fit with a Gaussian to extract the position μ_i and width σ_i of the electron peak. Finally, a functional form for the mean and standard deviation of the distributions is chosen to be a third order polynomial in momentum.

$$\mu(p) = \mu_0 + \mu_1 \cdot p + \mu_2 \cdot p^2 + \mu_3 \cdot p^3 \tag{4.3}$$

$$\sigma(p) = \sigma_0 + \sigma_1 \cdot p + \sigma_2 \cdot p^2 + \sigma_3 \cdot p^3 \tag{4.4}$$

Boundaries are constructed from this information by adding / subtracting n_σ from the mean. In the nominal case, we use $n_\sigma = 2.5$.

$$\begin{aligned} f_{max}(p) = \mu(p) + n_\sigma\sigma(p) = (\mu_0 + n_\sigma \cdot \sigma_0) + (\mu_1 + n_\sigma \cdot \sigma_1) \cdot p \\ (\mu_2 + n_\sigma \cdot \sigma_2) \cdot p^2 + (\mu_3 + n_\sigma \cdot \sigma_3) \cdot p^3 \end{aligned} \tag{4.5}$$

$$\begin{aligned} f_{min}(p) = \mu(p) - n_\sigma\sigma(p) = (\mu_0 - n_\sigma \cdot \sigma_0) + (\mu_1 - n_\sigma \cdot \sigma_1) \cdot p \\ +(\mu_2 - n_\sigma \cdot \sigma_2) \cdot p^2 + (\mu_3 - n_\sigma \cdot \sigma_3) \cdot p^3 \end{aligned} \tag{4.6}$$

Due to slight differences between the 6 sectors of the CLAS detector, this cut is calibrated and applied for each sector individually. The parameters of the cut polynomial are listed in table 4.3 The resulting cut for a 4 σ region in comparison to all negative tracks which survived the fiducial cuts is shown in figure 4.4 for the 6 sectors of CLAS.

4.1.6 Cut on the z-vertex position

For this analysis only primary scattered electrons are of interest, therefore only electron candidates which have a z-vertex $v_z \in$ [-27:7302, -22:6864] within the expected target region are accepted. This cut is applied after the

parameter	sector 1	sector 2	sector 3	sector 4	sector 5	sector 6
μ_3	-8.68739e-05	0.000459313	9.94077e-05	-0.000244192	-7.65218e-05	-0.000392285
μ_2	-0.000338957	-0.00621419	-0.00267522	-0.00103803	-0.00222768	-0.00105459
μ_1	0.0191726	0.0393975	0.02881	0.0250629	0.0233171	0.0265662
μ_0	0.2731	0.296993	0.285039	0.276795	0.266246	0.25919
σ_3	-0.000737136	0.000189105	-0.000472738	-0.000553545	-0.000646591	-0.000633567
σ_2	0.00676769	-0.000244009	0.00493599	0.00434321	0.00717978	0.00626044
σ_1	-0.0219814	-0.00681518	-0.0180929	-0.0140827	-0.0246181	-0.022029
σ_0	0.0474188	0.0475098	0.0461743	0.0492728	0.0546257	0.0517508

Table 4.3: Mean and σ values obtained from a slice fit of the momentum dependent sampling fraction.

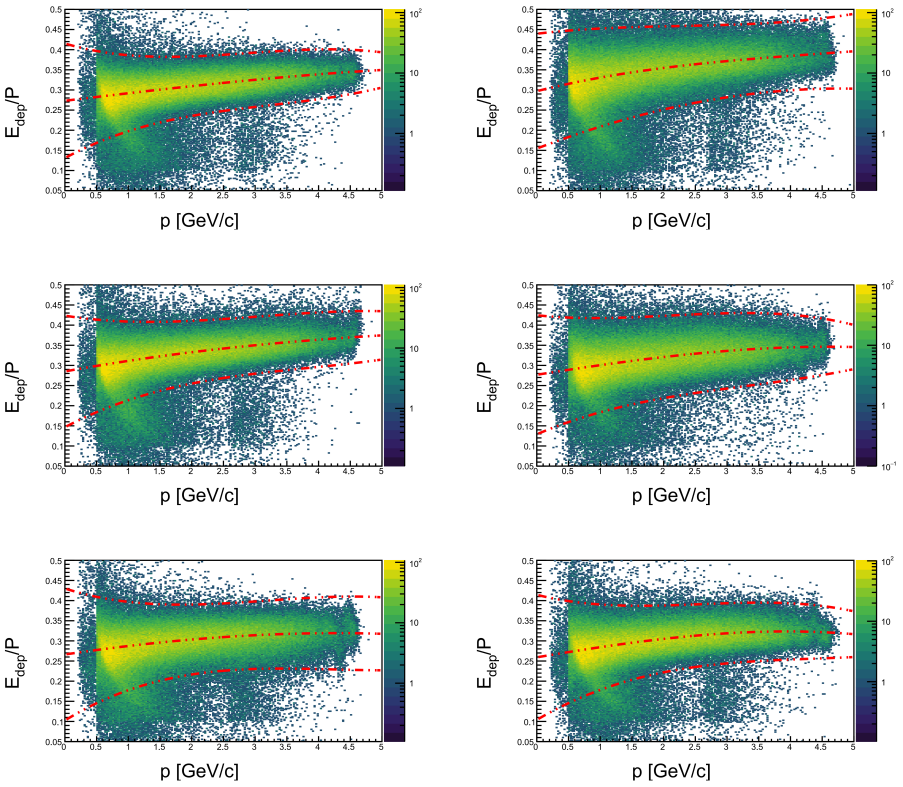

Figure 4.4: Sampling fraction cut for a 4 σ region in comparison to all negative tracks which survived the fiducial cuts

vertex position has been corrected (see the basic analysis section for more details).

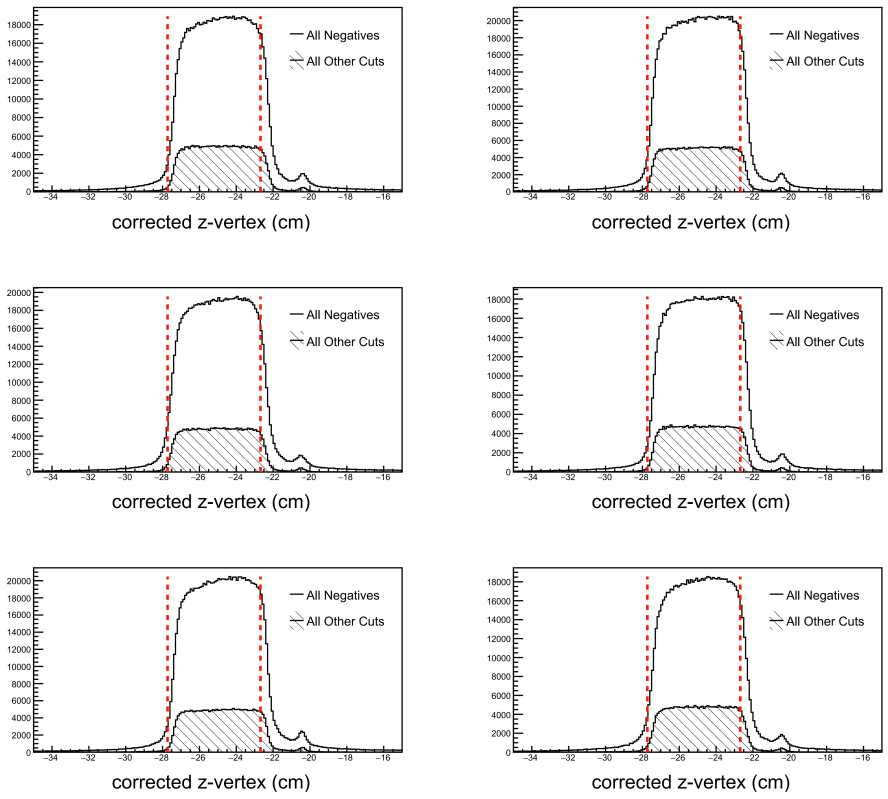

Figure 4.5: The track vertex cut is shown above. All negative tracks are shown in white, while the tracks passing all other criteria are shown in black hatch. The cut boundary is displayed as red lines. For e1-f the target center was located at -25 cm.

4.1.7 Cherenkov counter θ_{cc} and ϕ_{rel} matching to PMT cuts

As an additional criteria to reject "fake tracks" initiated by electronic noise and reconstruction uncertainties, the direct correlation between the polar angle measured at the Cherenkov counter θ_{cc} and the segment in which the track was detected can be used. Each half-sector of the CC contains 18 PMTs increasing in polar angle away from the beamline, these divisions are known as segments. From the ntuple22 data set of the raw data, they can be extracted as follows:

$$intsegment = event.cc\_segm[index]\%1000/10; \tag{4.7}$$

Additionally, PMTs that are placed on the left and right of the detector can be used to check consistency with the azimuthal angle the track forms with the central line of the detector. Figure 4.6 the definition of the azimuthal angle ϕ_{rel}. Per definition, $\phi_{rel} > 0$ means the track was in the

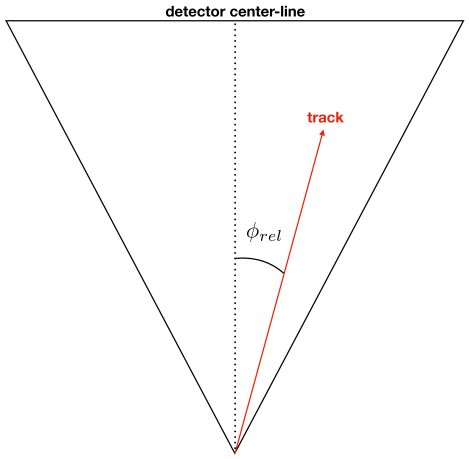

Figure 4.6: The angle ϕ_{rel} is the azimuthal angle between the central line of the detector and the track.

right half of the sector and $\phi_{rel} < 0$ means the track was in the left half of the sector. For this purpose, an integer value is defined by equation 4.8 to describe the PMT associated with the track.

$$intpmt = event.cc\_segm[index]/1000 - 1; \tag{4.8}$$

The left PMT is assigned value -1, the right 1, and a signal in both PMTs is assigned 0. If both PMTs have a signal, the track is allowed to pass. If the left PMT was the one that had a signal, only events with $\phi_{rel} < 0$ passes. Similarly if the right PMT fired (code = 1), only events with $\phi_{rel} > 0$ are allowed to pass. Figure 4.7 shows the correlation between θ_{CC} and the CC segment as well as the applied cut borders.

4.2 Hadron Identification

The hadron identification of CLAS6 is based on the time of flight information from the scintillation based time of flight counters (TOF). In addition a fiducial on the drift chambers region 1 is implemented to ensure the correct

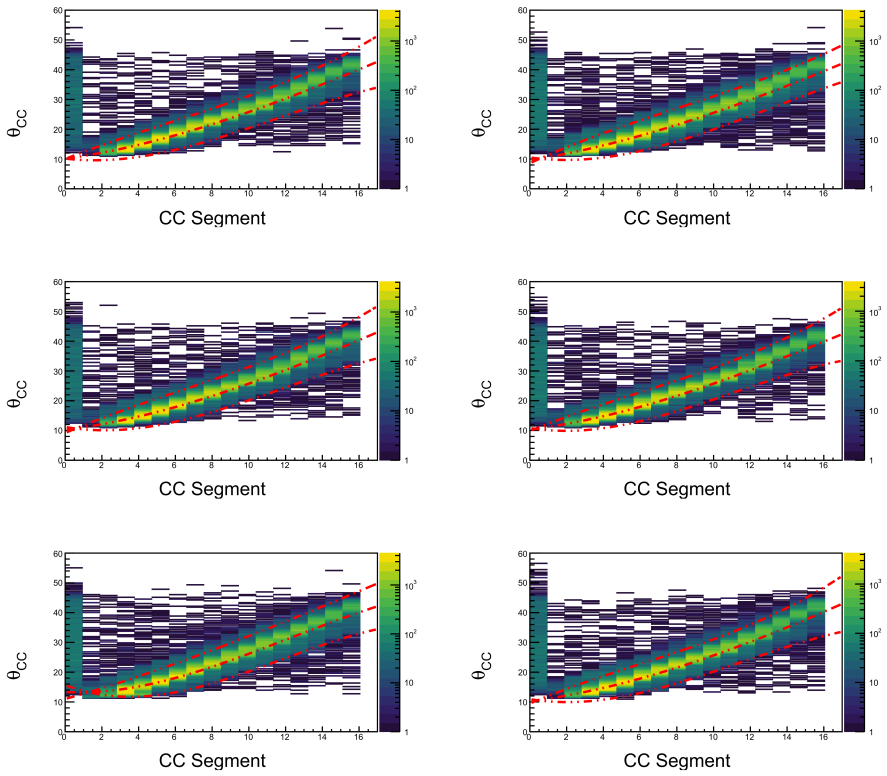

Figure 4.7: Correlation between θ_{CC} and the CC segment is shown above, with our selection boundaries (dashed red line).

momentum reconstruction of the hadron tracks. As an additional reconstruction check a cut on the vertex difference to the electron is used. For the final identification of the hadrons, a cut on the correlation between the TOF based beta value and the momentum of the tracks has been applied. For this purpose, different methods, like a simple 2 D cut and maximum likelihood assignment have been investigated. The later one is based on the discussion provided by the BES collaboration in [RGP09].

The cuts used for hadron classification are listed below and described in the following paragraphs.

- Drift chamber fiducial cut
- Hadron-electron vertex difference cut
- βvsp cut or likelihood maximization of $\beta(p, h)$

4.2.1 Drift chamber fiducial cut

A fiducial cut is applied to region 1 of the drift chambers using the same procedure as described for electrons. As a compromise between reconstruction efficiency and track quality, the fiducial cut for hadrons is only applied to region 1 of the DC. The parameters used for negative hadrons are the same which are used for electron. The parameters for positive tracks are h = 10 and $\theta = 60°$. Figure 4.8 shows the applied cut for the six sectors.

4.2.2 Hadron-electron vertex difference cut

Since the produced intermediate states investigated in this analysis have only a very short life time, no secondary vertexes are expected within the detector resolution. Therefore considering the vertex resolution, the hadron and the electron have to be produced at the same point. The distance between the electron vertex and the hadron candidate track vertex is computed (Δv_z = v_z^e - v_z^{had}). Considering the length of the target of 5 cm, the cuts in figure 4.9 have been applied in the six sectors.

4.2.3 β vs p cut and likelihood maximization of $\beta(p, h)$

Both methods which have been used for the hadron particle ID are based on the momentum dependence of the β value of the track, which has been obtained from the time of flight measurement. In this section, positive hadrons are used as an example. The same method is applied to negative hadrons.

Determination of the experimental mean and resolution values of the β versus p correlations

As a first step for the hadron identification, the momentum dependent mean and standard deviation of the β versus p correlations have to be determined for the different particles. In the case where exceptionally accurate Monte Carlo (MC) simulations of the detector are available, one can use the truth information and track matching to construct the β vs. p 2-dimensional histograms, and fit the $\mu(p)$ and $\sigma(p)$. In the absence of high quality MC, analysts typically fit directly the spectrum of β vs. p and extract the mean and variance. In this work, an enhanced sample of candidates for each of the three positive particles in question is created before doing the fitting. In this way, the extracted values are less influenced by contamination. For fitting of pion and proton resolutions, positive tracks are assumed to be pions and

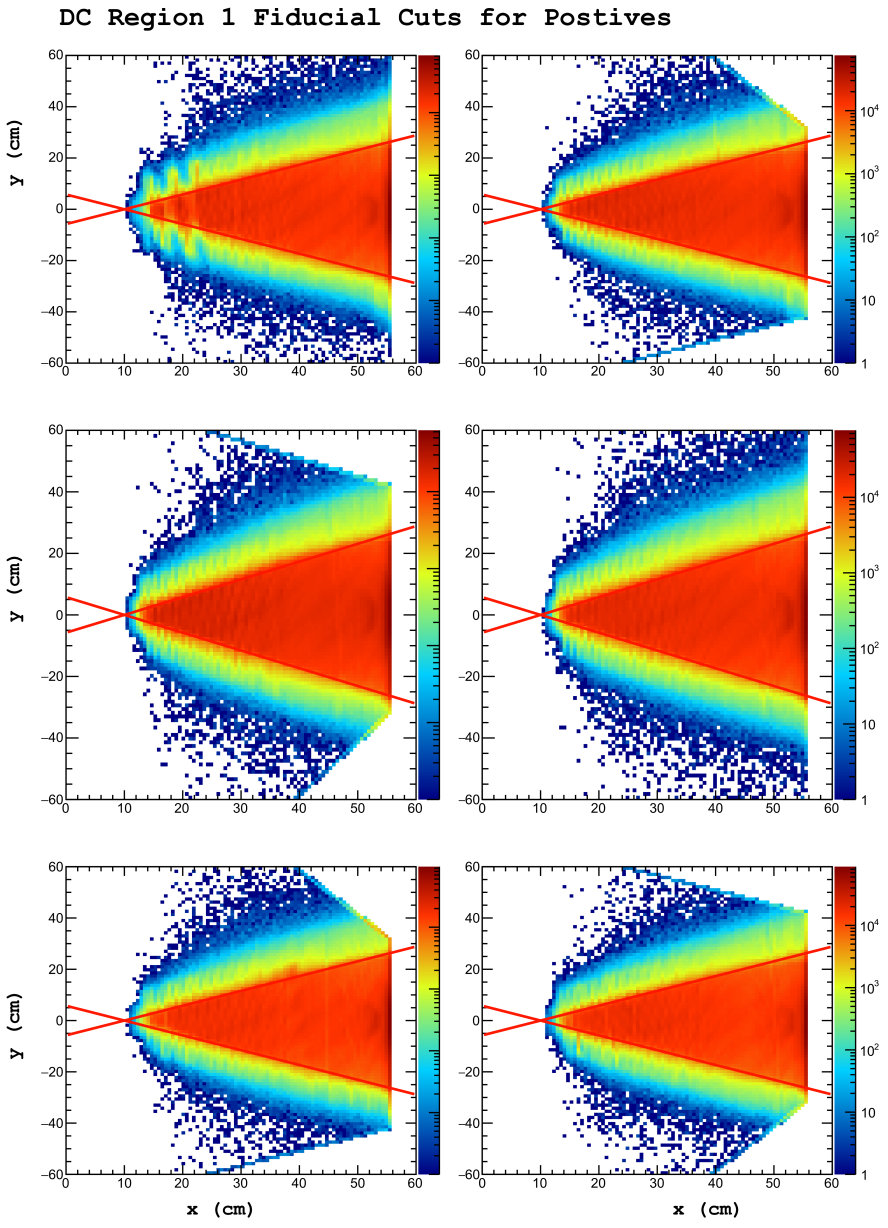

Figure 4.8: Hits of positive tracks on region 1 of the drift chambers in the six sectors, events falling between the red lines pass the fiducial cut.

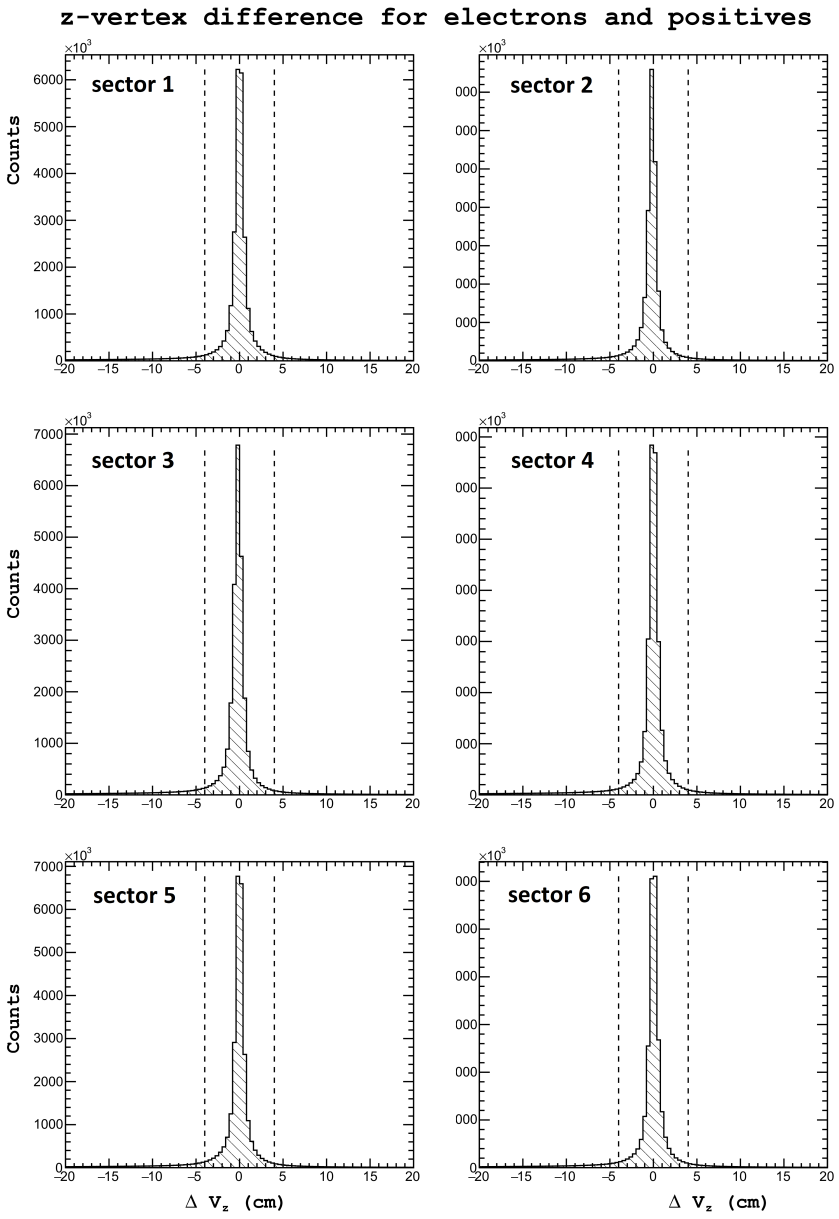

Figure 4.9: Shown above: The difference between the z-vertex position between detected electrons and positive tracks.

the missing mass of the event is calculated. Then, a cut is placed around

the neutron mass.

With this method, two main exclusive reactions are selected. The first is $ep \to e\pi^+ N$, and the second is $ep \to ep\pi^0$. In this way most positrons, and positive kaons are removed from the sample prior to fitting. The mean and variance are fit using a third order polynomial in p (MINUIT χ^2 minimization is used). Negative pions and kaons are fit directly (as is normally done). The parametrization used for the mean $\mu(p,h)$ and resolutions $\sigma(p,h)$ are:

$$\mu(p,h) = \mu_{theory} + \Delta\mu \tag{4.9}$$

$$\mu_{theory} = \frac{1}{\sqrt{1+\left(\frac{m_h}{p}\right)^2}} \tag{4.10}$$

$$\Delta\mu = \mu_0 + \mu_1 \cdot p + \mu_2 \cdot p^2 \tag{4.11}$$

$$\sigma(p,h) = \sigma_0 + \sigma_1 \cdot p + \sigma_2 \cdot p^2 \tag{4.12}$$

The values for the single particles are displayed in table 4.4.

hadron	par.	sector 1	sector 2	sector 3	sector 4	sector 5	sector 6
K^+	μ_2	0.00111554	-8.97687e-05	4.78796e-05	0.000376425	-0.00204856	0.000652209
K^+	μ_1	-0.00468038	6.19414e-05	-0.00081741	-0.00107931	0.00629181	-0.00264143
K^+	μ_0	0.00361012	0.00134921	0.00299674	0.00220194	0.000117821	0.00162582
K^+	σ_2	-0.000331838	-0.00105807	-0.000712404	-0.000573934	-0.000259289	0.000508389
K^+	σ_1	-0.00105857	0.00236686	0.000509169	0.000163467	-0.00233617	-0.00461598
K^+	σ_0	0.0154964	0.0117702	0.0140748	0.0143761	0.0184055	0.0180945
π^+	μ_2	-0.000962041	-0.000300602	-0.000306326	-3.2245e-05	-0.00226511	-0.000330818
π^+	μ_1	0.00296349	0.0016512	0.0021962	0.00176045	0.00750862	0.00126443
π^+	μ_0	-0.00225794	-0.00047045	0.000370406	0.000435526	-0.000449409	-0.00131045
π^+	σ_2	-0.000127659	0.000691895	-0.000289961	0.000315041	-0.000936521	-0.000131269
π^+	σ_1	-0.000489092	-0.0033948	0.00196853	-0.00197841	0.00212778	-0.000339411
π^+	σ_0	0.0155195	0.0167998	0.0124066	0.0157476	0.0145571	0.0141728
p^+	μ_2	-0.00039358	-0.000701003	-0.000347651	0.0004854	-0.00121666	0.000563786
p^+	μ_1	-0.000295423	0.00170899	0.000794901	-0.000744446	0.00376887	-0.00353545
p^+	μ_0	0.00227353	0.00231676	0.00364672	0.00276859	0.00128827	0.00439605
p^+	σ_2	0.001429	0.00144256	0.00124456	0.00190709	0.00141039	0.0011516
p^+	σ_1	-0.0021472	-0.00262226	-0.00196308	-0.00385218	-0.00186708	-0.00186749
p^+	σ_0	0.0107541	0.0109091	0.0104381	0.0115449	0.0109969	0.0107759
π^-	μ_2	3.28823666e-04	-1.30673670e-05	-2.32502052e-04	-9.75619848e-04	-5.89834444e-04	5.27496718e-04
π^-	μ_1	-3.94924663e-03	-2.66028661e-03	-1.28565631e-03	9.09410075e-04	-2.01610684e-03	-4.42276918e-03
π^-	μ_0	9.48011169e-04	1.55078786e-03	1.43431985e-03	1.35056935e-03	4.59833580e-03	2.30751866e-03
π^-	σ_2	4.37635504e-04	4.38306224e-04	5.32057510e-04	3.36999845e-04	7.74135462e-04	1.36515196e-04
π^-	σ_1	-3.28011836e-03	-3.28456104e-03	-3.82847286e-03	-3.11749323e-03	-4.63110728e-03	-2.21229710e-03
π^-	σ_0	1.63296567e-02	1.62229164e-02	1.59769911e-02	1.58803427e-02	1.74670064e-02	1.51753145e-02
K^-	μ_2	-2.72020947e-03	-5.21081786e-03	-2.13868763e-02	-4.45600034e-03	-7.60703841e-03	-5.27074813e-03
K^-	μ_1	1.78610401e-02	2.30787460e-02	9.49357818e-02	1.95764575e-02	3.63245785e-02	2.92417500e-02
K^-	μ_0	-2.26190100e-02	-2.22562379e-02	-1.02704771e-01	-2.25931014e-02	-5.10484618e-02	-3.19918187e-02
K^-	σ_2	1.76905114e-02	1.62989708e-02	3.60928130e-02	1.51270521e-02	1.91308107e-02	2.38470033e-02
K^-	σ_1	-7.74901862e-02	-7.33041628e-02	-1.57454534e-01	-7.26870393e-02	-9.23654247e-02	-1.02397836e-01
K^-	σ_0	1.07082820e-01	1.00573410e-01	1.93148260e-01	1.00993689e-01	1.26963814e-01	1.30057621e-01

Table 4.4: Parameters obtained for the mean and σ value for the hadronic bands in the β versus p distribution.

Figure 4.10 shows the fitted $\mu(p)$ and $\mu(p) \pm \sigma(p)$ for protons, π^+ and K^+.

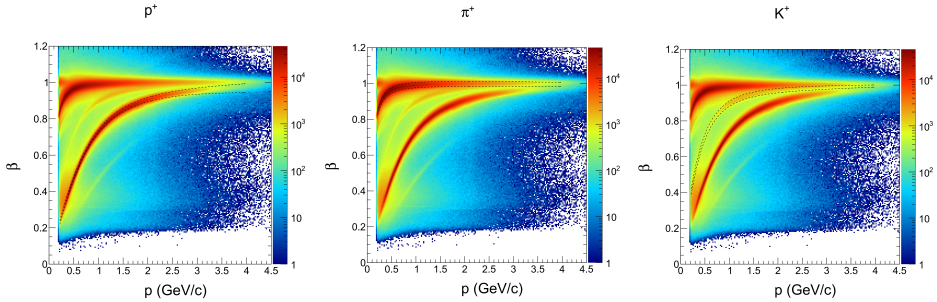

Figure 4.10: All positive tracks overlaid with the borders of $\mu(p) \pm \sigma(p)$ for protons, π^+ and K^+

2 dimensional cuts on the β versus p correlations

The easiest method to select the different hadrons is a 2 dimensional cut on the β versus p correlations based on the fitted values for $\mu(p)$ and $\sigma(p)$. To achieve a high efficiency, typically a 3 $\sigma(p)$ cut is used. However to increase the purity especially at higher particle momenta, a narrower cut (i.e. 2 or 2.5 $\sigma(p)$) can be applied. Depending on the size of the cut range it has to be considered, that the bands of the different particles start to overlap between 2 and 3.5 GeV. At higher energies tracks are assigned multiple time to different species.

Likelihood maximization of $\beta(p, h)$

While a double assignment caused by a 2 dimensional cut on the β versus p correlations is less problematic in exclusive reaction, since most of the wrongly assigned particles are rejected by the exclusivity cuts, it is a serious problem for semi inclusive reactions. However also in exclusive reactions it can increase the background and decrease the purity of the sample, especially if missing mass cuts are applied.

Therefore a likelihood maximization of $\beta(p, h)$ has been implemented as an alternative particle ID. With this method, a normalized probability density function $P(x, p, h)$ for each particle species considered, is constructed for each input into the likelihood analysis. Here, x corresponds to the feature being used to categorize different particles (in our case, x is the β value measured by CLAS time-of-flight), p is the particle momentum, and h is the

hadron being hypothesized (e.g.: the possible values for positive hadrons are pion, kaon, proton). In general if one uses a set of N variables x = (x_1, x_2, ..., x_N), the likelihood for a hypothesis h is defined as:

$$L_h = \prod_{i=1}^{N} P_i(x_i, p, h) \tag{4.13}$$

In our case, the only random variable we consider is β, and the likelihood is just the PDF. Here, and in many cases where the choice is statistically appropriate, it is possible to use a Gaussian PDF for the variable x_i (here β).

$$P(\beta, p, h) = \frac{1}{\sqrt{2\pi} \cdot \sigma_\beta(p,h)} \cdot exp\left(-\frac{1}{2} \cdot \left(\frac{\beta - \mu_\beta(p,h)}{\sigma_\beta(p,h)}\right)^2\right) \tag{4.14}$$

The identity is assigned by choosing the particle hypothesis h which maximizes the likelihood ratio:

$$\frac{L_h}{L_{\pi^+} + L_{K^+} + L_p} \tag{4.15}$$

Using this method, every positive track is assigned to a particle exactly one time. However, since not all possible particles are considered as a possible hypothesis (i.e. positrons), the likelihood value can be quite small when compared with the maximum likelihood for that species. In this case a wrong particle or a badly reconstructed track would be assigned. To avoid these situations, the confidence level

$$\alpha = 1 - \int_{\mu-\beta}^{\mu+\beta} P(\beta, p, h) d\beta \tag{4.16}$$

of each track is calculated and a cut is applied on the minimum confidence. This cut can be easily varied to see how it changes the analysis result.

This quantity represents the probability to observe a value of β as far or farther from the mean as β_{obs}. Confidence levels close to zero correspond to tracks which are poorly identified as the class h. In the case that the PDF is Gaussian, the standard 1, 2, and 3 σ cuts on β vs. p can be understood simply as confidence levels of approximately 0.32 = 1-0.68, 0.05 = 1-0.95, and 0.01 = 1-0.99. Figure 4.11 shows the distribution of confidence level for π^+, K^+ and protons after being classified by the likelihood ratio.

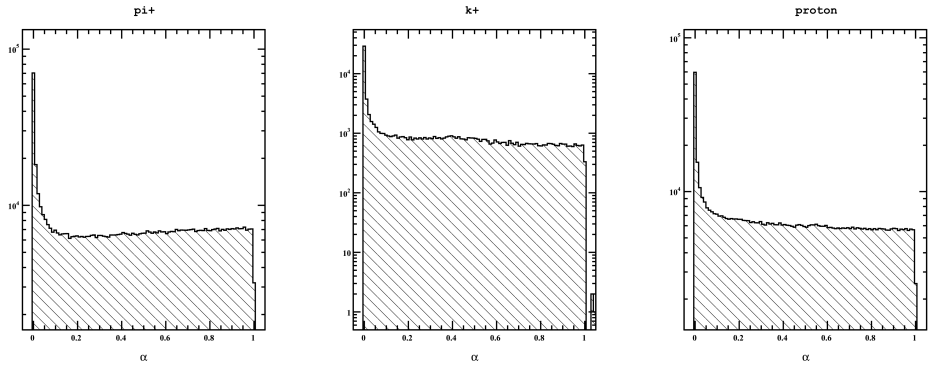

Figure 4.11: Distribution of confidence level for π^+, K^+ and protons after being classified by the likelihood ratio.

Chapter 5

Analysis of the Beam Spin Asymmetry

5.1 Introduction

The beam spin asymmetry has been determined for positive pions from the channel $ep \rightarrow e'\pi^+(n)$. By dividing the electron-pion events into several bins of different independent kinematic variables, the beam spin asymmetry has been determined for different average values of the kinematic variables. For each kinematic bin, the structure function ratio $A_{LU}^{sin(\phi)}$ has been extracted. Due to the limited statistics, the values of $A_{LU}^{cos(\phi)}$ and $A_{LU}^{cos(2\phi)}$ can not be extracted explicitly. However their influence on $A_{LU}^{sin(\phi)}$ has been considered in the study of the systematic error.

5.2 Event selection

After particle identification is applied, events with exactly one identified trigger electron and one identified π^+ are selected. Since the study aims on the deeply inelastic region, only events with $W > 2$ and $Q^2 > 1$ are considered for the analysis. To select the exclusive $e'\pi^+(n)$ sample, a 3 σ cut around the neutron peak within the $e'\pi^+X$ missing mass spectrum has been performed. Figure 5.1 (left) shows the $e'\pi^+X$ missing mass spectrum and the applied cut. The selected region is shown in red color.

The comparison of the peak area and the background distribution in figure 5.1 (right) shows, that after a strict particle ID, the background is at a level of only $\approx$ 10% for a 3 σ cut. A systematic study of the cut

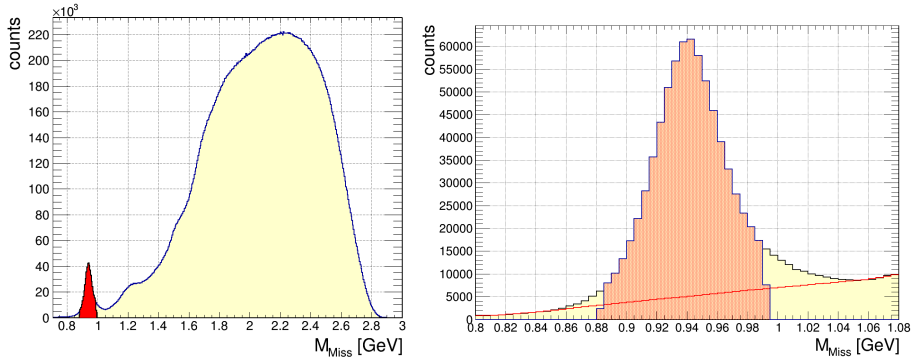

Figure 5.1: Left: Missing mass spectrum of $e\text{'}\pi^+X$ (yellow) and selected events within a 3 σ region around the missing neutron peak (red). Right: Zoomed and re-binned view of the missing neutron peak of $e\text{'}\pi^+X$ and estimated background contribution (red line)

with around the missing neutron peak will show that the influence of the background on the beam spin asymmetry is unelectable.

5.3 Kinematics and Binning

5.3.1 Kinematics

For a first overview, the momentum and angular distributions of the detected electron and pion after the application of the event selection cuts are given in figure 5.2, 5.3 and 5.4.

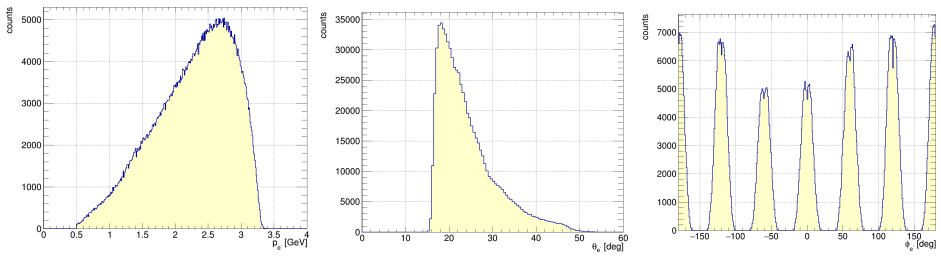

Figure 5.2: Momentum, θ and ϕ distributions of electrons of the selected events.

With the applied missing mass cut, the Q^2 versus W correlation shown in figure 5.5 has been obtained.

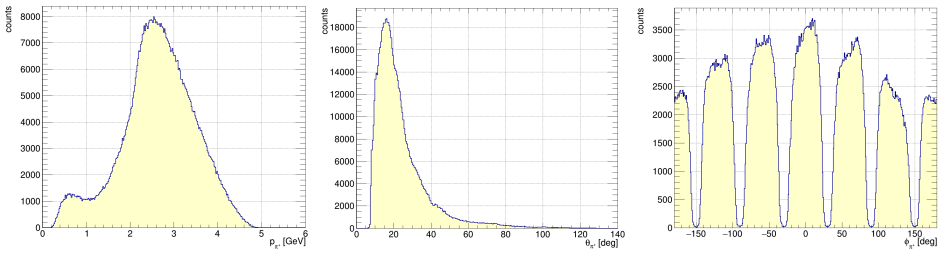

Figure 5.3: Momentum, θ and ϕ distributions of positive pions of the selected events.

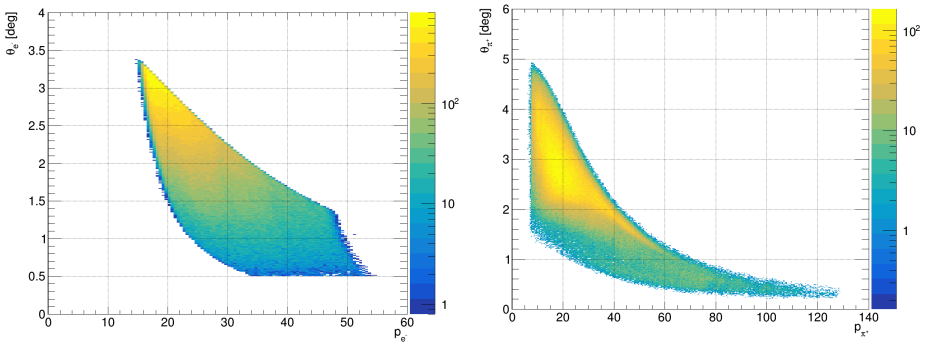

Figure 5.4: Correlation between momentum and θ angle for electrons (left) and positive pions (right).

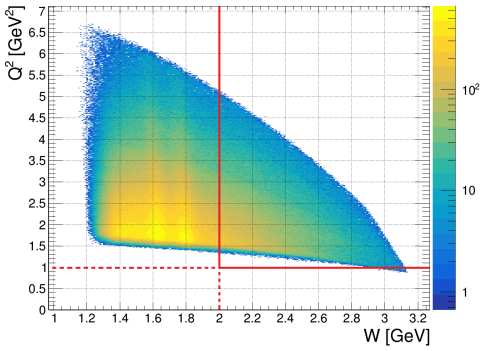

Figure 5.5: Q^2 vs W distributions for events which fulfill the missing mass cut. The cut to selected the deep inelastic (DIS) region is shown as red lines.

The beam spin asymmetry measurement has been performed for the independent kinematic variables $-t$, Q^2 and x. For comparison to theoretical

calculations, also the dependence on $-u$ has been determined. Figure 5.6 shows the correlation between the different variables.

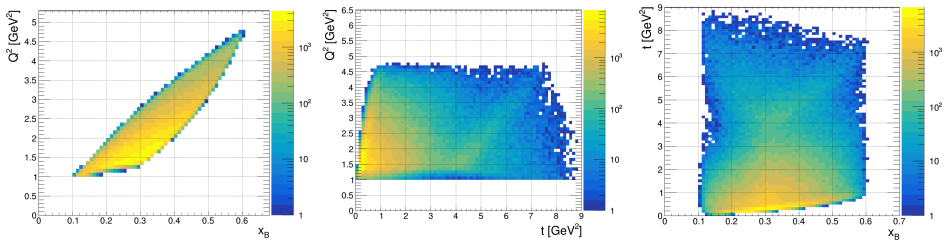

Figure 5.6: Correlation between the kinematic variables $-t$, Q^2 and x for the exclusive $e\pi^+(n)$ events.

To get a better estimation of the available statistics, figure 5.7 and 5.8 show the one dimensional projection of the 3 variables as well as the distribution of $-u$.

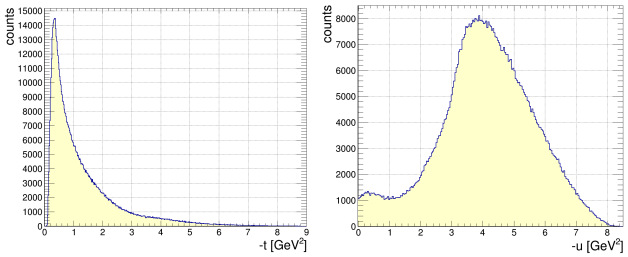

Figure 5.7: One dimensional projection of the kinematic variables $-t$ and $-u$ for the exclusive $e\pi^+(n)$ events.

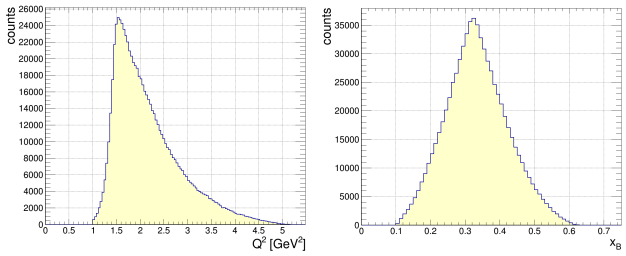

Figure 5.8: One dimensional projection of the kinematic variables Q^2 and x_B for the exclusive $e\pi^+(n)$ events.

To enable a better visualization of the kinematics, also the dependence

on $cos(\theta_{CM})$ is studied, which is directly correlated with $-t$ and $-u$. Figure 5.9 shows the distribution of $cos(\theta_{CM})$ and its correlation to $-t$ and $-u$ as well as the correlation between $-t$ and $-u$.

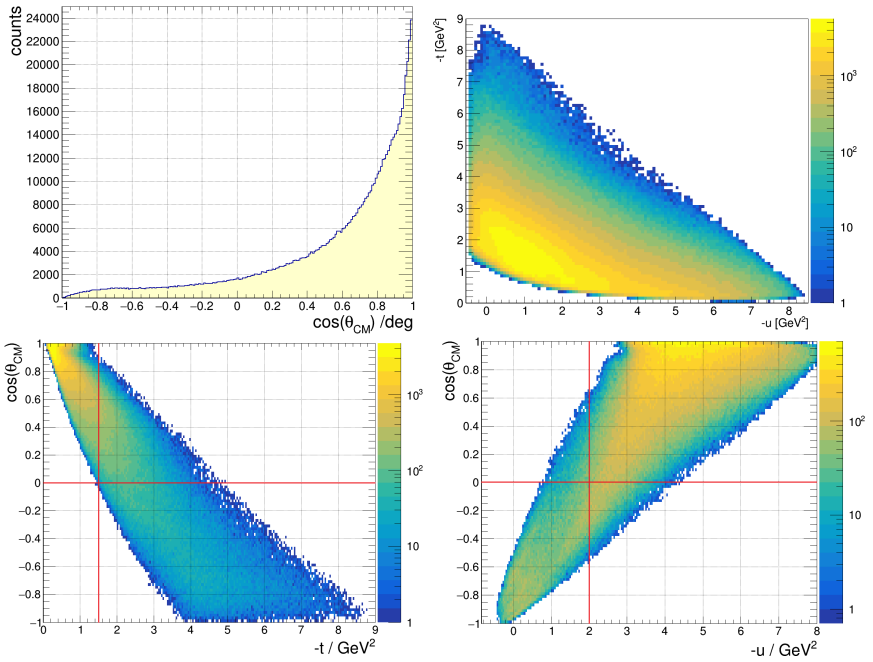

Figure 5.9: Upper row: Distribution of $cos(\theta_{CM})$ (left) and correlation between $-t$ and $-u$ (right). Lower row: Correlation of $cos(\theta_{CM})$ to $-t$ (left) and $-u$ (right).

The figure nicely visualizes, that the pions are strongly focused in forward directions (small $-t$, large $-u$). In addition a direct correlation between $-t$ as well as $-u$ and $cos(\theta_{CM})$ can be observed.

For the extraction of the BSA in Q^2 and x_B a separation of the events according to the direction of the produced positive pions has been performed. The backward direction is defined as events with $cos(\theta_{CM}) < 0$ and $-u < 2$, while the forward direction is defined as $cos(\theta_{CM}) > 0$ and $-t < 1.5$. The cuts are visualized by red lines in figure 5.9. With this cuts, the distributions and correlation for Q^2 and x_B shown in figure 5.10 and 5.11 have been obtained in backward and forward directions.

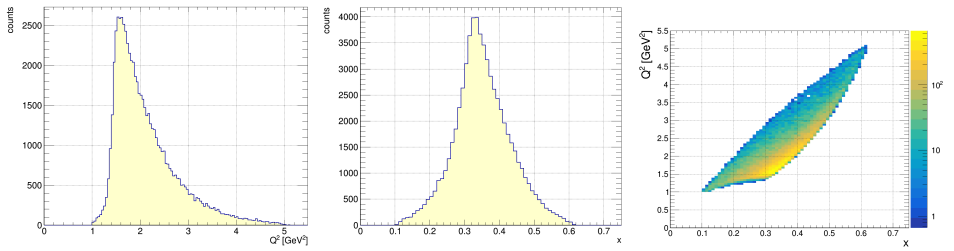

Figure 5.10: Distribution and Correlation of Q^2 and x_B for events with a pion in backward direction.

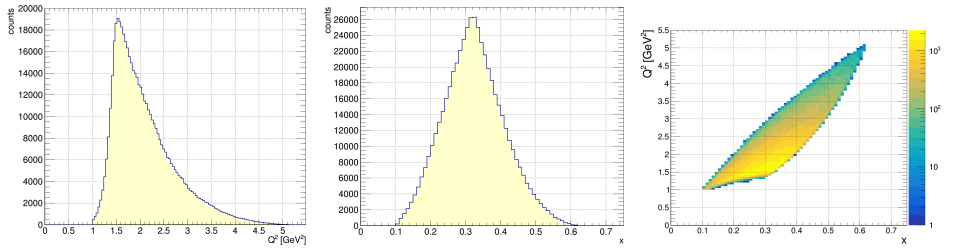

Figure 5.11: Distribution and Correlation of Q^2 and x_B for events with a pion in forward direction.

5.3.2 Binning

As a compromise between statistics in each bin and the quality of the beam spin asymmetry fit, 12 equally distributed bins between -180 and 180 degrees in ϕ have been chosen. Figure 5.12 shows a typical ϕ distribution.

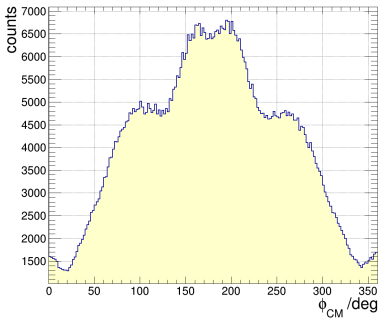

Figure 5.12: Typical distribution of ϕ_{CM}

For the other variables the binning has been adjusted according to the

available statistics and the expected change of the BSA with a variation of the variable. It was especially aimed to keep a minimum number of events in each bin, to ensure a proper BSA extraction. This consideration led to 12 bins in $-t$, 6 bins in q^2 and 7 bins in x. Figure 5.13 shows the selected bins for the different variables.

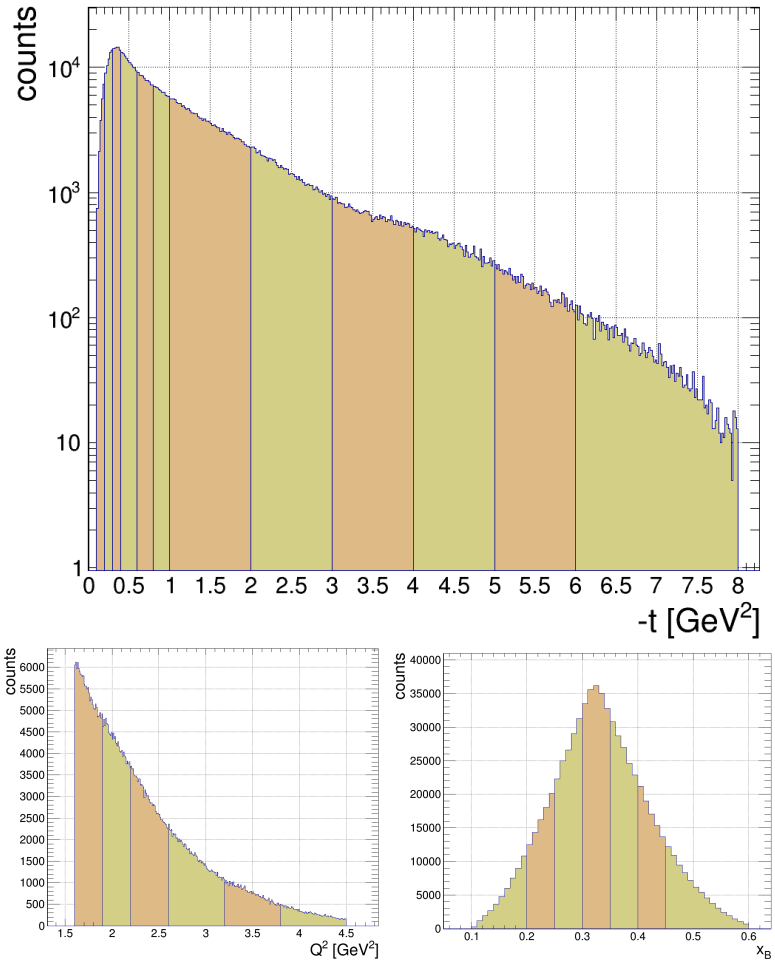

Figure 5.13: Bins selected for $-t$, q^2 and x_B.

Table 5.1 gives the bin range, as well as the mean value for the different kinematic variables in the specified bin for the $-t$ bins.

Table 5.2 gives the bin range, as well as the mean value for the different kinematic variables in the specified bin for the Q^2 bins.

Table 5.3 gives the bin range, as well as the mean value for the different

$-t$ range	$\langle -t \rangle$	$\langle -u \rangle$	$\langle Q^2 \rangle$	$\langle x_B \rangle$
0.1 - 0.2	0.1677	5.756	1.458	0.2042
0.2 - 0.3	0.2545	5.031	1.694	0.262
0.3 - 0.4	0.3498	4.652	1.896	0.3069
0.4 - 0.6	0.4936	4.706	2.147	0.3382
0.6 - 0.8	0.6956	4.731	2.279	0.3467
0.8 - 1.0	0.8962	4.551	2.28	0.3451
1.0 - 2.0	1.425	3.978	2.273	0.3476
2.0 - 3.0	2.421	2.918	2.339	0.3613
3.0 - 4.0	3.459	1.695	2.293	0.3654
4.0 - 5.0	4.443	0.9755	2.313	0.3638
5.0 - 6.0	5.435	0.8219	2.599	0.3661
6.0 - 8.0	6.671	0.6442	2.699	0.3343

Table 5.1: Bin range and mean value for the different kinematic variables in the specified bin for the $-t$ bins.

Q^2 range	$\langle Q^2 \rangle$ b	$\langle -t \rangle$ b	$\langle -u \rangle$ b	$\langle x_B \rangle$ b	$\langle Q^2 \rangle$ f	$\langle -t \rangle$ f	$\langle -u \rangle$ f	$\langle x_B \rangle$ f
1.6 - 1.9	1.742	3.575	1.002	0.2172	1.743	0.6267	4.26	0.2927
1.9 - 2.2	2.042	3.91	0.984	0.3523	2.043	0.6724	4.504	0.3266
2.2 - 2.6	2.381	4.276	0.9591	0.3882	2.382	0.7238	4.747	0.3634
2.6 - 3.2	2.859	4.806	0.9208	0.4322	2.858	0.7936	5.111	0.4084
3.2 - 3.8	3.455	5.381	0.9029	0.4816	3.456	0.8833	5.48	0.4627
3.8 - 4.5	4.097	5.964	0.8427	0.5326	4.071	0.9808	5.751	0.5188

Table 5.2: Bin range and mean value for the different kinematic variables in the specified bin for the Q^2 bins for pion going in the backward (b) and forward (f) region.

kinematic variables in the specified bin for the x_B bins.

5.4 Extraction of the BSA

For each kinematic bin, the BSA is extracted separately and fitted with the theoretical function to determine $A_{LU}^{sin(\phi)}$. While the statistical error is directly determined by the fit, the systematic error has been studied by varying the different systematic uncertainties like the borders of the particle ID cuts and the uncertainty of the beam polarization.

x_B range	$\langle x_B \rangle$ b	$\langle -t \rangle$ b	$\langle -u \rangle$ b	$\langle Q^2 \rangle$ b	$\langle x_B \rangle$ f	$\langle -t \rangle$ f	$\langle -u \rangle$ f	$\langle Q^2 \rangle$ f
0.1 - 0.2	0.1684	6.129	0.9646	1.354	0.1701	0.5856	6.2	1.36
0.2 - 0.25	0.2282	4.901	1.021	1.582	0.2273	0.552	5.271	1.605
0.25 - 0.3	0.2786	3.971	1.041	1.681	0.2765	0.5944	4.591	1.772
0.3 - 0.35	0.3258	3.502	0.9932	1.793	0.3246	0.6619	4.133	1.95
0.35 - 0.4	0.3732	3.759	0.9705	2.133	0.3732	0.7327	4.25	2.307
0.4 - 0.45	0.4227	4.195	0.9371	2.579	0.4224	0.8026	4.494	2.737
0.45 - 0.6	0.4959	5.037	0.8834	3.409	0.4924	0.9216	4.965	3.476

Table 5.3: Bin range and mean value for the different kinematic variables in the specified bin for the x_B bins for pion going in the backward (b) and forward (f) region.

5.4.1 Determination of the parameter $A_{LU}^{sin(\phi)}$ and statistical errors

In each bin i the beam spin asymmetry (here A_i) is calculated according to,

$$A_i = \frac{1}{P_e} \cdot \frac{N_+^i - N_-^i}{N_+^i + N_-^i} \tag{5.1}$$

where P_e is the average electron beam polarization over the data set. It has been measured during the beam time to 74.9 $\pm$ 2.4%. The symbols $N_\pm^i$ represent the number of events counted in bin i with helicity $\pm$.

The uncertainty on the measured value of A_i can be attributed to statistical uncertainty on the counts $N_i^\pm$, and the uncertainty associated with the measurement of P_e. The statistical uncertainty reported on the measurement includes the contribution from counts, but not from the uncertainty in P_e which is included in the systematic errors. In general, the uncertainty in a measured observable x depends on the uncertainty of the parameters (here denoted by $\vec{\theta}$) used to construct it $\vec{\theta}$ in the following way.

$$\sigma_x^2 = \sum_{i=1}^{N} \sum_{j=1}^{N} \frac{\partial x}{\partial \theta_i} \frac{\partial x}{\partial \theta_j} \rho_{ij} \sigma_i \sigma_j \tag{5.2}$$

For the beam spin asymmetry in the i^{th} bin A_i one finds that without correlations ($\rho_{ij} = \delta_{ij}$) the error propagation proceeds as shown below.

$$\sigma_A^2 = \frac{A^2}{P_e^2} \cdot \sigma_{P_e}^2 + \frac{4 \cdot (N_-^2 \sigma_+^2 + N_+^2 \sigma_-^2}{P_e^2 \cdot (N_+ + N_-)^4} \tag{5.3}$$

The first term which is the contribution from the variance in the measurements of beam polarization will be included as a systematic error. The second term is used as the statistical error bars shown through the analysis. The counts $N_i^{\pm}$ for the i^{th} bin are assumed to be Poisson in nature, and therefore have a variance equal to the expected number of counts $\sigma_{\pm}^2 = N_i^{\pm}$. With this expression for the statistical uncertainty on the counts, and dropping the beam polarization term for now, the expression becomes:

$$\sigma_A = \sqrt{\frac{4 \cdot N_+ \cdot N_-}{P_e^2 \cdot (N_+ + N_-)^3}} \tag{5.4}$$

Figure 5.14 shows the beam spin asymmetry as a function of ϕ fitted with the in a first order approximation expected function $BSA = A_{LU}^{sin(\phi)} \cdot sin(\phi)$ for the single $-t$ bins.

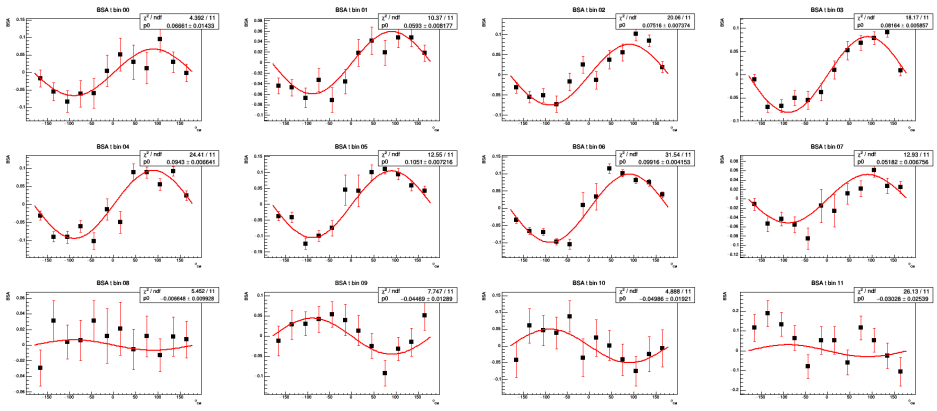

Figure 5.14: Beam spin asymmetry as a function of ϕ fitted with the in a first order approximation expected function $BSA = A_{LU}^{sin(\phi)} \cdot sin(\phi)$ for the single $-t$ bins.

The extracted moment $A_{LU}^{sin(\phi)}$ as a function of $-t$ is shown in figure 5.15.

Figure 5.16 shows the beam spin asymmetry as a function of ϕ fitted with the in a first order approximation expected function $BSA = A_{LU}^{sin(\phi)} \cdot sin(\phi)$ for the single Q^2 bins in backward and forward direction.

The extracted moment $A_{LU}^{sin(\phi)}$ as a function of Q^2 in backward and forward direction is shown in figure 5.17.

Figure 5.18 shows the beam spin asymmetry as a function of ϕ fitted with the in a first order approximation expected function $BSA = A_{LU}^{sin(\phi)} \cdot sin(\phi)$ for the single x_B bins in backward and forward direction.

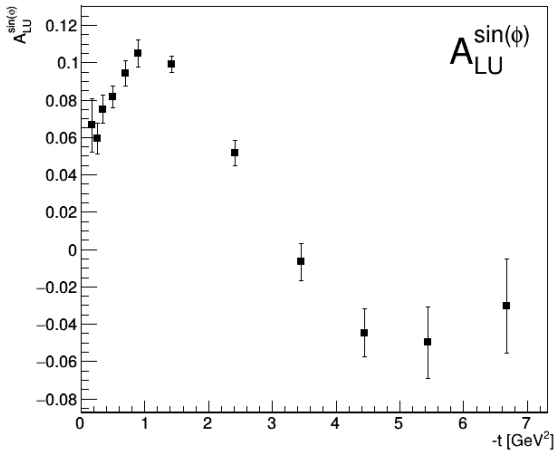

Figure 5.15: $A_{LU}^{sin(\phi)}$ as a function of $-t$.

The extracted moment $A_{LU}^{sin(\phi)}$ as a function of x_B in backward and forward direction is shown in figure 5.19.

5.4.2 Estimation of systematic errors

In addition to statistical errors, which are determined by the available statistics and which can be only influenced by the choice of the binning, also systematic errors have to be taken into account. Systematic effects are shifts or biases in the measured result of different observable as a result of the procedure used in the measurement.

Many systematic effects can be identified and corrected. However, in the cases where an effect cannot be completely removed, the degree to which the correction for the effect is uncertain is included in the result of the measurement as a systematic uncertainty. Table 5.4 summarizes the sources of systematic uncertainty considered in this analysis.

In addition to the effects listed in table 5.4, also the the influence of the inclusion of the $cos(\phi)$ and $cos(2\phi)$ term into the fit function on the value of $A_{LU}^{sin(\phi)}$ has been studied and included as a systematic uncertainty. Since the low statistics and the resulting large statistical error of the BSA in the single ϕ bins does not allow a fit of all 3 momenta, the fit has been performed on the one side with setting $A_{LU}^{cos(\phi)}$ and $A_{LU}^{cos(2\phi)}$ to 0, as it is done for the standard extraction method of $A_{LU}^{sin(\phi)}$ and on the other side under the condition, that only the $cos(\phi)$ momentum gives a contribution

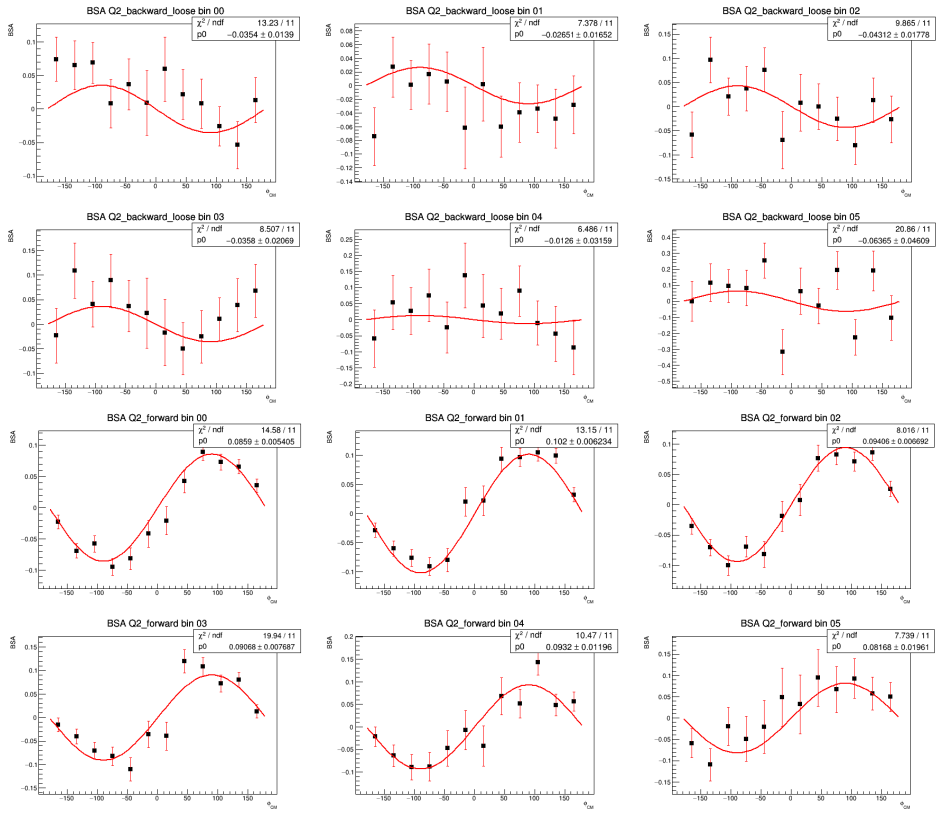

Figure 5.16: Beam spin asymmetry as a function of ϕ fitted with $BSA = A_{LU}^{sin(\phi)} \cdot sin(\phi)$ for the single Q^2 bins in backward and forward direction.

and the $cos(2\phi)$ momentum is set to 0. Figure 5.20 shows the obtained result. The figure shows, that the inclusion of the second order momentum has no significant influence on the results of $A_{LU}^{sin(\phi)}$.

However, it can be observed, that due to the relatively low statistics in the ϕ bins, $A_{LU}^{cos(\phi)}$ tends to be fitted with unreasonably high values, therefore two more iterations have been performed, in which $A_{LU}^{cos(\phi)}$ is was limited to maximal values of 0.1 and 0.2. In another study, all 3 momenta have been included under the condition, that the $cos(\phi)$ and $cos(2\phi)$ momenta are both limited to 0.1 and in a second iteration to 0.2. Since they are expected to be smaller than $A_{LU}^{sin(\phi)}$, already a limit of 0.1 should give a reasonable estimation of their effect on $A_{LU}^{sin(\phi)}$. The effect will be shown on the example of the $-t$ binning.

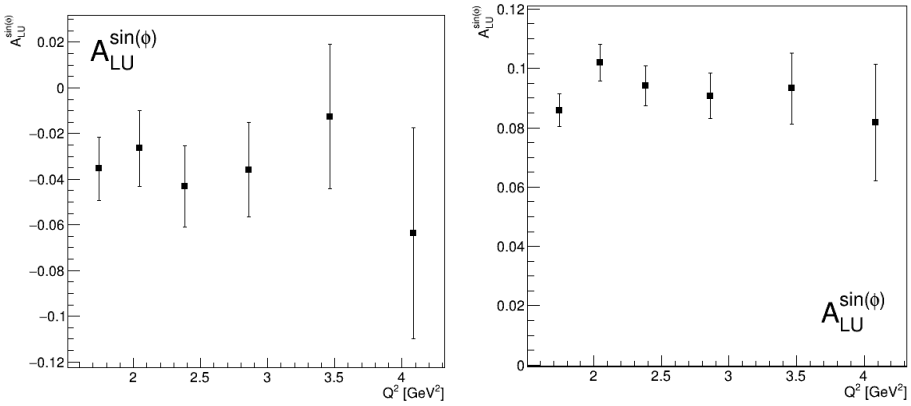

Figure 5.17: $A_{LU}^{sin(\phi)}$ as a function of Q^2 in backward direction (left) and forward direction (right).

source	variation
beam polarization	± 0.024
DC region 1 fiducial	± 1 cm
DC region 3 fiducial	± 3 cm
EC - w fiducial	± 10 cm (1 bar)
EC - v fiducial	± 10 cm (1 bar)
EC - u fiducial	± 10 cm (1 bar)
EC sampling fraction	± 1σ
z-vertex	± 0.5 cm
θ_{CC} matching	± 1σ
EC energy deposition	± 0.01 (GeV)
pion confidence level (α)	0.01 - 0.07
missing neutron mass cut	± 1σ

Table 5.4: Different sources of systematic errors considered in this analysis and their considered systematic variation uncertainty.

The BSA fits, considering additional terms of the full equation

$$BSA = \frac{\sigma^+ - \sigma^-}{\sigma^+ + \sigma^-} = \frac{A_{LU}^{sin(\phi)} \cdot sin(\phi)}{1 + A_{LU}^{cos(\phi)} \cdot \cdot cos(\phi) + A_{LU}^{cos(2\phi)} \cdot \cdot cos(2\phi)} \tag{5.5}$$

for the $-t$ bins under different conditions are given in figure 5.21. The extracted momenta for the case that all 3 momenta are included are shown

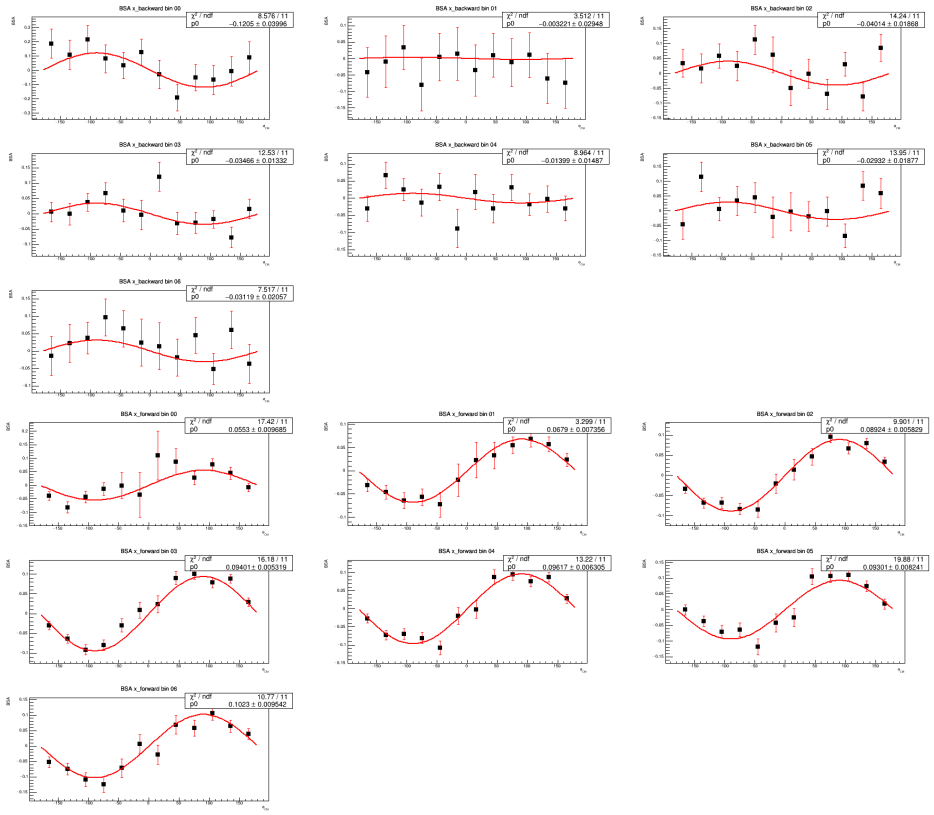

Figure 5.18: Beam spin asymmetry as a function of ϕ fitted with $BSA = A_{LU}^{sin(\phi)} \cdot sin(\phi)$ for the single x_B bins in backward and forward direction.

in figure 5.22.

It can be observed, that also in this case many of the absolute values for $A_{LU}^{cos(\phi)}$ and $A_{LU}^{cos(2\phi)}$ try to tend to be unnaturally large and therefore reach the fit limit. In addition nearly all values have statistical errors, which exceed the magnitude of the value significantly. Nevertheless, it can be observed, that the influence of their inclusion into the fit on $A_{LU}^{sin(\phi)}$ is smaller than the statistical error of the $A_{LU}^{sin(\phi)}$ values and as figure 5.23 illustrates also smaller than the total systematic error of all other sources and does therefore not influence the observed behavior or the significance of the results at all.

To include the error in the total systematic error, the variation between the fit of all 3 momenta with a limit of 0.1 and the original fit is taken as an additional systematic error source.

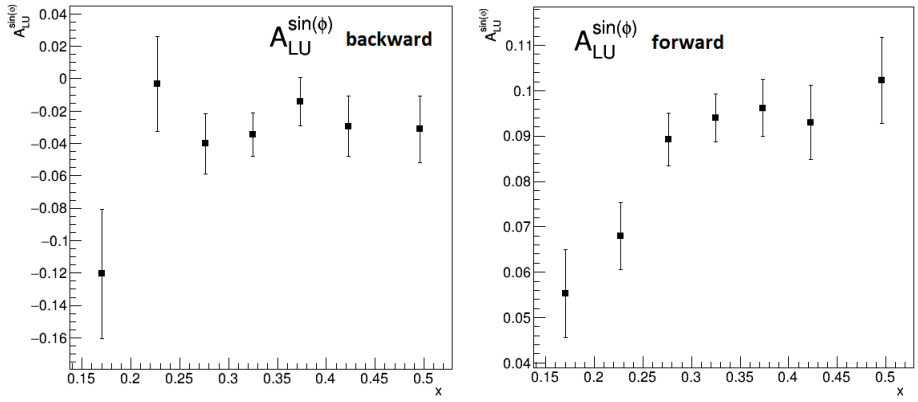

Figure 5.19: $A_{LU}^{sin(\phi)}$ as a function of x in backward direction (left) and forward direction (right).

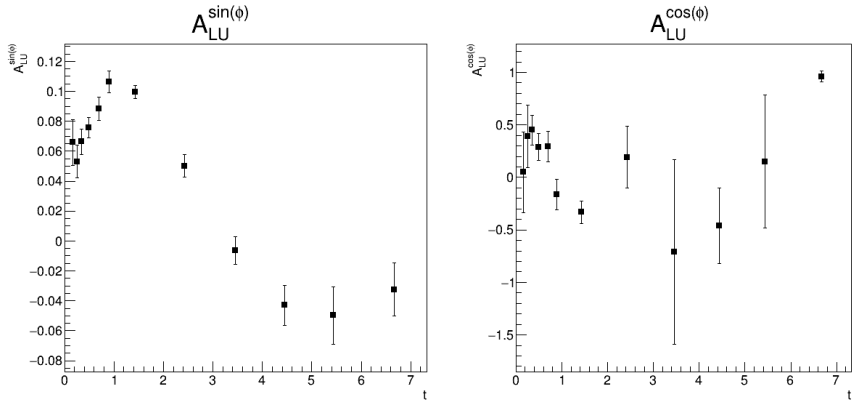

Figure 5.20: Extracted parameters for $A_{LU}^{sin(\phi)}$ and $A_{LU}^{cos(\phi)}$ with $A_{LU}^{cos(2\phi)}$ set to 0 and no limitations.

The errors are determined individually for each bin and for each source. Figure 5.24 gives an overview of the systematic error contribution of the different sources.

To obtain the total systematic error of a specific bin, the systematic errors of the single source are added quadratically in this bin. The obtained systematic errors are listed in the following tables:

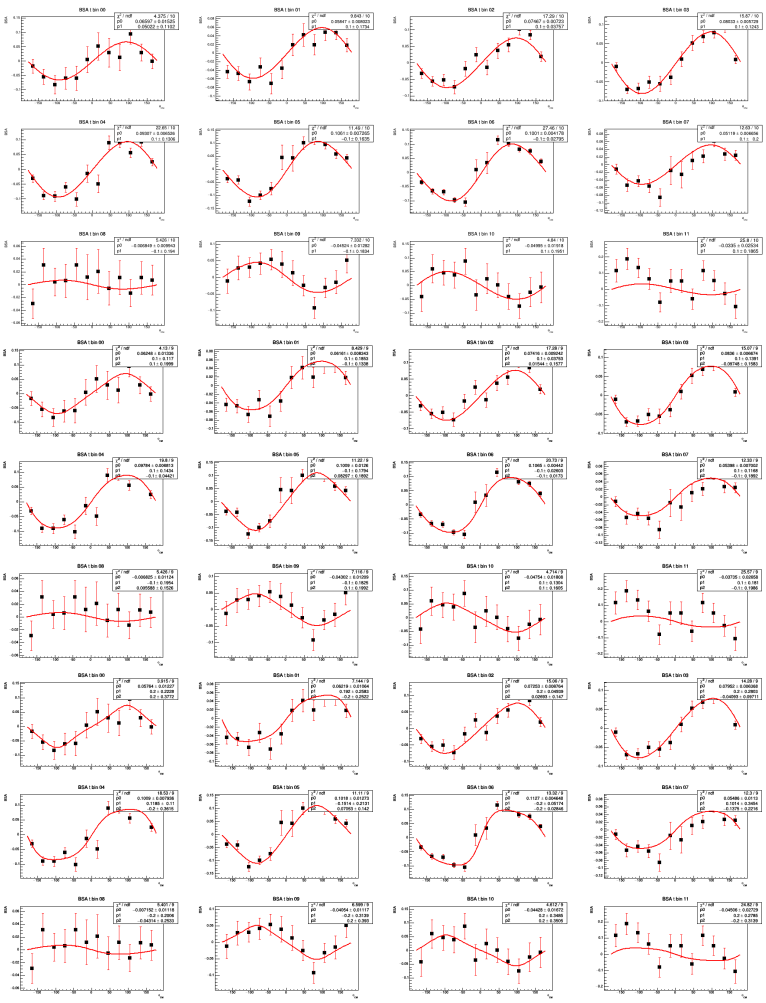

Figure 5.21: Fits of the BSA in the single $-t$ bins, if $A_{LU}^{cos(2\phi)}$ is set to 0 and $A_{LU}^{cos(\phi)}$ limited to 0.1 (upper group)and if all 3 momenta are included with a limit of $A_{LU}^{cos(\phi)}$ and $A_{LU}^{cos(2\phi)}$ of 0.1 (middle group) and 0.2 (lower group).

5.4.3 Results and Discussion

The figures 5.25, 5.26 and 5.27 show the final results for the $A_{LU}^{sin(\phi)}$ momentum, including the statistical and systematic errors.

The $-t$ dependence of $A_{LU}^{sin(\phi)}$ shows a clear transition from positive values up to 0.12 for small $-t$ to negative values of up to -0.5 for larger $-t$ values. The transition happens around $-t = 3GeV^2$ which corresponds to

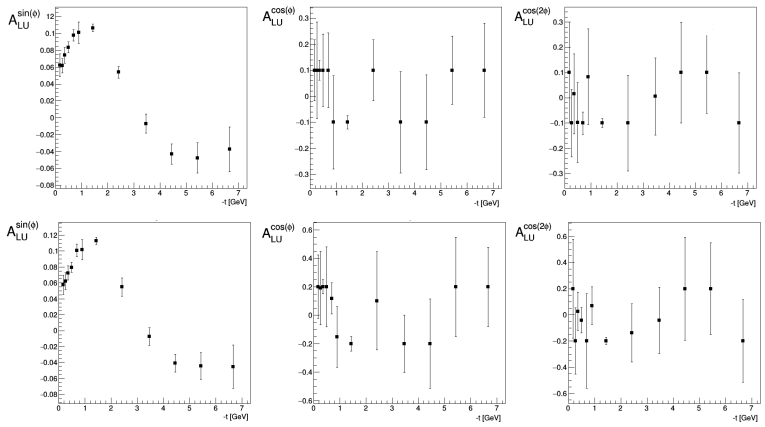

Figure 5.22: Extracted parameters for $A_{LU}^{sin(\phi)}$, $A_{LU}^{cos(\phi)}$ and $A_{LU}^{cos(2\phi)}$ with a limit for the later two of 0.1 (upper plots) and 0.2 (lower plots).

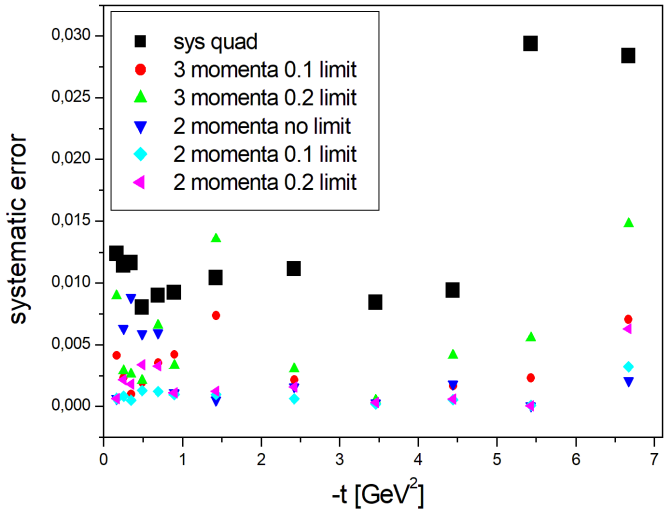

Figure 5.23: Systematic error caused by different configurations of the BSA fit in relation to the total systematic error of all other sources (black rectangles).

$cos(\theta_{CM}) = 0$ or $\theta_{CM} = 90°$ and therefore marks the transition between π^+ emitted in forward and backward direction. The forward direction and especially the region of small $-t$ values can be theoretically described by generalized parton distributions (GPD), while the region of large $-t$ or equivalently

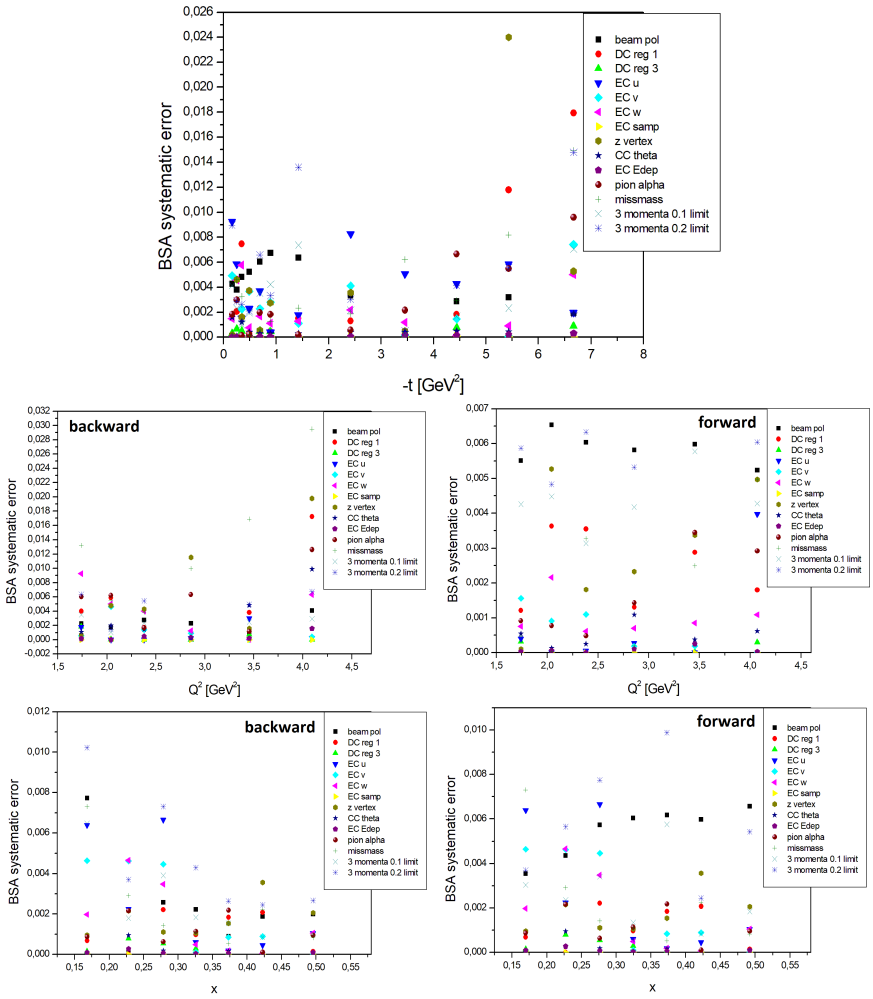

Figure 5.24: Systematic error contribution of the different identified sources on the value of $A_{LU}^{sin(\phi)}$ for $-t$ bin (upper row), Q^2 bin with the pions going in backward and forward direction (middle row) and for x_B bins with pions in backward and forward direction (lower row).

small $-u$ values follows the theoretical description of transition distribution amplitudes (TDA). By making accurate measurements over a wide range of Q^2 and t, we can explore the transition from the hadronic to partonic reaction mechanisms.

By selecting small $-u$ and small $-t$ values, the two region scan be separated. This clear separation is visualized for the Q^2 and x_B binning, which

$\langle -t \rangle$	value	stat. err	sys. err
0.17	0.0666	0.0143	0.0124
0.25	0.0593	0.0082	0.0114
0.35	0.0752	0.0074	0.0117
0.49	0.0816	0.0059	0.0081
0.70	0.0943	0.0066	0.0090
0.90	0.1051	0.0072	0.0092
1.43	0.0992	0.0042	0.0104
2.42	0.0518	0.0068	0.0112
3.46	-0.0066	0.0099	0.0084
4.44	-0.0447	0.0129	0.0094
5.44	-0.0499	0.0192	0.0294
6.67	-0.0303	0.0254	0.0284

Table 5.5: List of statistical and systematic errors of $A_{LU}^{sin(\phi)}$ for the different $-t$ bins.

$\langle Q^2 \rangle$ b	value b	stat. err b	sys. err b	$\langle Q^2 \rangle$ f	value f	stat. err f	sys. err f
1.742	-0.0354	0.0139	0.0184	1.743	0.0859	0.0054	0.0074
2.042	-0.0265	0.0165	0.0135	2.043	0.1020	0.0062	0.0105
2.381	-0.0431	0.0178	0.0085	2.382	0.0941	0.0067	0.0086
2.859	-0.0358	0.0207	0.0168	2.858	0.0907	0.0077	0.0079
3.455	-0.0126	0.0316	0.0185	3.456	0.0932	0.0120	0.0104
4.097	-0.0637	0.0461	0.0434	4.071	0.0817	0.0196	0.0111

Table 5.6: List of statistical and systematic errors of$A_{LU}^{sin(\phi)}$ for the different Q^2 bins for pions going to backward (b) and forward (f) directions.

nicely reflect the sign change between the backward and forward region of the pion production.

$\langle x_B \rangle$ b	value b	stat. err b	sys. err b	$\langle x_B \rangle$ f	value f	stat. err f	sys. err f
0.1684	-0.1205	0.0400	0.0149	0.1701	0.0553	0.0097	0.0120
0.2282	-0.0032	0.0295	0.0084	0.2273	0.0679	0.0074	0.0096
0.2786	-0.0401	0.0187	0.0103	0.2765	0.0892	0.0058	0.0114
0.3258	-0.0347	0.0133	0.0037	0.3246	0.0940	0.0053	0.0066
0.3732	-0.0140	0.0149	0.0038	0.3732	0.0962	0.0063	0.0091
0.4227	-0.0293	0.0188	0.0052	0.4224	0.0930	0.0082	0.0077
0.4959	-0.0312	0.0206	0.0036	0.4924	0.1023	0.0095	0.0074

Table 5.7: List of statistical and systematic errors of $A_{LU}^{sin(\phi)}$ for the different x_B bins for pions going to backward (b) and forward (f) directions.

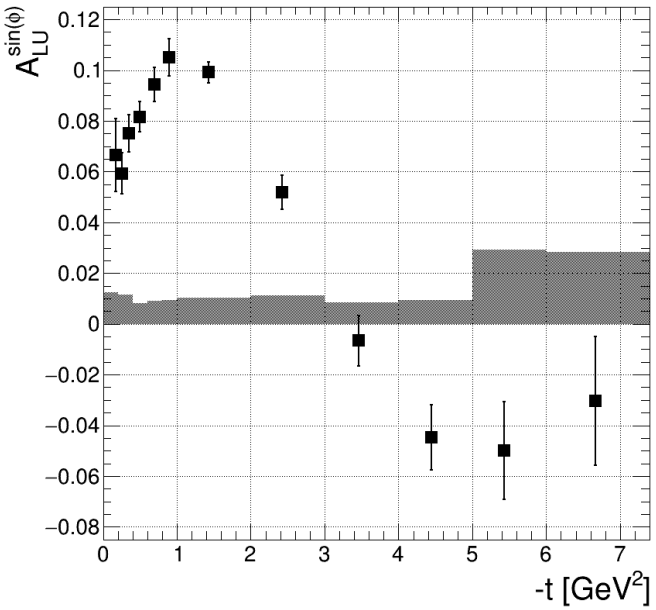

Figure 5.25: $A_{LU}^{sin(\phi)}$ for different $-t$ bins. The shaded area represents the systematic error of the bin.

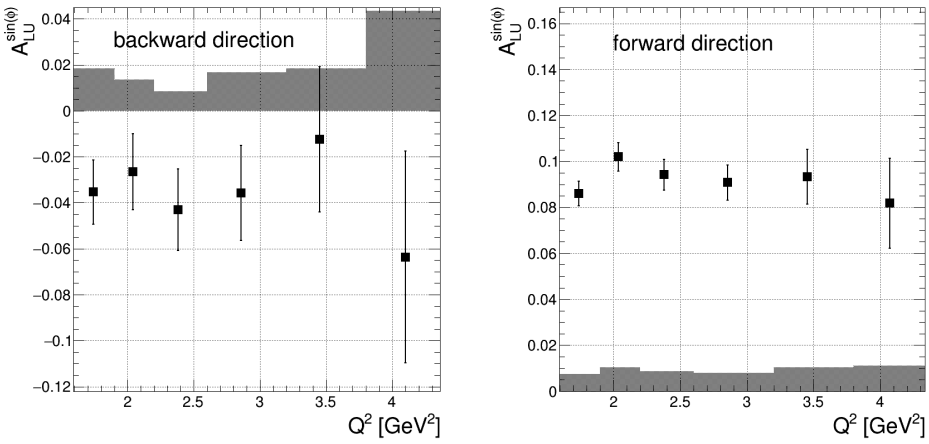

Figure 5.26: $A_{LU}^{sin(\phi)}$ for different Q^2 bins for pions going in backward direction (left plot) and for pions going in forward direction (right plot). The shaded area represents the systematic error of the bin.

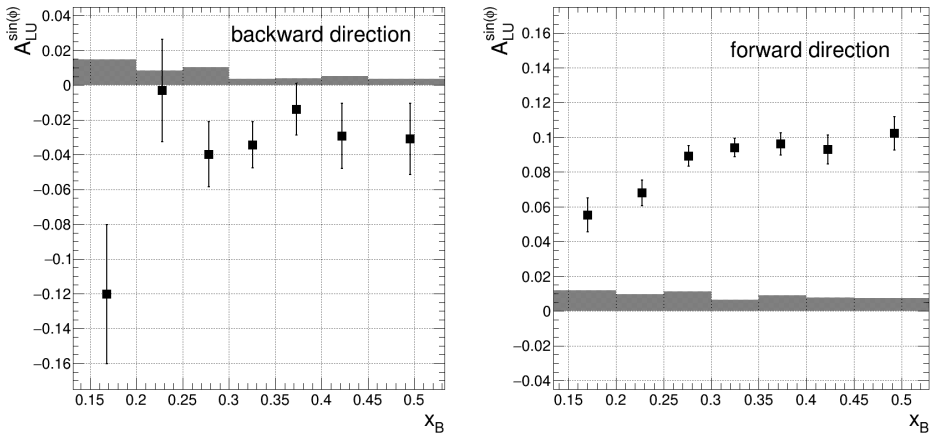

Figure 5.27: $A_{LU}^{sin(\phi)}$ for different x_B bins for pions going in backward direction (left plot) and for pions going in forward direction (right plot). The shaded area represents the systematic error of the bin.

Bibliography

[PGG18] K. Park et al., Physics Letters B 780, 340-345 (2018).

[CWL01] C. W. Leemann et al., Ann. Rev. Nucl. Part. Sci. 51, 413 (2001).

[YCC11] Y. C. Chao et al., J. Phys. Conf. Ser. 299, 012015 (2011).

[MDM00] M. D. Mestayer et al., Nucl. Instrum. Meth. A449, 81 (2000).

[GA01] G. Adams et al., Nucl. Instrum. Meth. A465, 414 (2001).

[ESS99] E. S. Smith et al., Nucl. Instrum. Meth. A432, 265 (1999).

[MA01] M. Amarian et al., Nucl. Instrum. Meth. A460, 239 (2001).

[NAH10] N. A. Harrison, Exploring the Structure of the Proton via Semi-Inclusive Pion Electroproduction, Ph.D. thesis, Connecticut U. (2010).

[MM] M. Mirazita, "Kinematic corrections for e1-f".

[RGP09] R.-G. Ping et al., Int. J. Mod. Phys. A24S1, 23 (2009).